MONKES: a fast neoclassical code for the evaluation of monoenergetic transport coefficients

F. J. Escoto[1]**, J. L. Velasco**[1]**, I. Calvo**[1]**, M. Landreman**[2] **and F. I. Parra**[3]

[1]Laboratorio Nacional de Fusión, CIEMAT, 28040 Madrid, Spain
[2]University of Maryland, College Park, MD 20742, USA
[3]Princeton Plasma Physics Laboratory, Princeton, NJ 08540, USA

E-mail: `fjavier.escoto@ciemat.es`

April 2023

Abstract. MONKES is a new neoclassical code for the evaluation of monoenergetic transport coefficients in large aspect ratio stellarators. The code is spectral in spatial and velocity coordinates, and employs a block tridiagonal algorithm for solving the resultant linear system of equations. It is shown that MONKES is accurate and efficient. In particular, the calculation of monoenergetic coefficients by MONKES, in a single processor, is sufficiently fast for its integration in stellarator optimization suites.

1. Introduction

Stellarators are three-dimensional magnetic confinement devices which are promising candidates for a fusion reaction power plant. In order to achieve magnetic confinement of fusion plasmas, Poincaré-Hopf theorem requires that (to have non-vanishing magnetic fields), the field lines must be tangent to a topologically toroidal surface called flux surface [1]. In addition, magnetic field lines must have the so called rotational transform, which means that, when following a magnetic field line, the line rotates both in the toroidal and poloidal directions. For stellarators, such magnetic field can be created entirely by external magnets. In contrast, tokamaks rely on the current driven by the plasma to generate rotational transform, which makes them intrinsically non-steady and more prone to magnetohydrodynamic instabilities. Thus, stellarators are potentially an attractive alternative to the tokamak concept for a fusion power plant. However, tokamaks posses a property which stellarators lack: axisymmetry. This additional symmetry implies, as a consequence of Noether's theorem, that collisionless orbits of all charged particles in the magnetic field experience a zero secular radial drift. That is, when their movement is averaged, they remain in the same flux surface in which they were born and therefore are well confined. In a tokamak, the main neoclassical mechanism of particle loss is due to collisions, which alter their otherwise confined trajectories. On the other hand, in a stellarator, magnetic geometry interplays with collisions enhancing radial neoclassical transport. Hence, stellarator magnetic fields must be neoclassically optimized to improve their confinement properties. The most general class of stellarators which shares the tokamak property of zero secular radial drift is the omnigenous stellarator. Two different subclasses of omnigenous stellarator have drawn much attention in the past and recent years: quasi-symmetric (QS) and quasi-isodynamic (QI) stellarators. Examples of the former subclass are the Helically Symmetric eXperiment (HSX) or the unfinished National Compact Stellarator Experiment (NCSX). The neoclassical properties of QS stellarators are isomorphic to those in an equivalent tokamak [2], [3], and by means of stellarator optimization it is possible to design magnetic fields with extremely low neoclassical losses [4]. Of the latter subclass, the Wendelstein 7-X (W7-X) experiment was conceived to be close to QI and demonstrates [5] that theoretically based stellarator optimization can be applied to construct a device with much better confinement properties than any of the previously built three-dimensional machines. Quasi isodynamic configurations have the additional property (besides omnigeneity) that contour lines of constant magnetic field strength in a flux surface close poloidally.

This constraint has an important implication: QI stellarators produce zero bootstrap current to first order in a low collisionality expansion [6], [7]. Bootstrap current makes the magnetic configuration sensitive to plasma pressure and its effect should be taken into account to ensure that the stellarator good confinement is robust throughout all of its modes of operation. For instance, for stellarators with an island divertor, it can bring the chain of islands to inner radial positions [8]. Hence, from the non symmetric omnigenous configurations, the QI concept has drawn most of the attention and enormous effort has been put in obtaining stellarators sufficiently close to QI [9], [cite JL robust optimization paper], [10], [11], [12]. Other non-QI omnigenous configurations have recently been investigated [13] and it remains unclear whether magnetic fields of this category can be as robust to plasma pressure effects as QI ones.

In order to improve the neoclassical confinement properties of stellarators, the straightforward approach is to include the relevant quantities to be minimized as targets in optimization suites. Ideally, one would obtain these targets by solving the most general drift-kinetic equation possible, which is five dimensional. However, solving such equation is not an easy task and in general takes too much time to be numerically solved, making this approach not feasible in practice. Neoclassical properties are typically addressed indirectly or by solving simplified versions of the drift-kinetic equation. The latter approach has been successfully applied to produce quick calculations of radial fluxes of energy and particles. We give two examples of this success. Based on the rigorous derivations for low collisionality of [14] and [15] for almost omnigenous and large aspect ratio stellarators respectively, two bounce averaged drift-kinetic equations are solved very fast by the code `KNOSOS` [16], [17]. For the $1/\nu$ regime, the code `NEO` [18] computes the effective ripple ϵ_{eff}, which is a figure of merit for radial transport. Both of these codes are included in the stellarator optimization suite `STELLOPT` [19]. In what regards to parallel transport, the long mean free path formulas for flow and bootstrap current such as the ones given in [20], [21] or [22] have been used in the optimization process that lead to W7-X. However, although they can be computed very fast and might capture some qualitative behaviour, these formulae are plagued with noise due to resonances in rational surfaces and even with smoothing ad hoc techniques, they are not accurate [23]. Therefore, an accurate calculation of the bootstrap current is required to understand precisely how it is affected by other parameters of the magnetic field for optimization purposes. With the solely exception of precisely QS stellarators [23] (for which analytical formulae for

tokamaks are applicable), accurate calculations of the bootstrap current could not be calculated sufficiently fast and have been excluded of the optimization process in the past.

In this work we present MONKES (MONoenergetic Kinetic Equation Solver), a new neoclassical code conceived to satisfy the necessity of taking into account the bootstrap current effect in stellarator optimization suites. Specifically, MONKES makes possible to use as target monoenergetic geometric coefficient $\widehat{D}_{31}$ (its precise definition is given in section 2), which is related to the bootstrap current. This coefficient has a role of the driving force for the spontaneous parallel particle and heat flows in a neoclassical theory which uses a model momentum conserving collision operator [24]. Nevertheless, the code can be used not only for optimization purposes but as a replacement for the standard and successful neoclassical code DKES [25]. The paper is organized as follows: In section 2 the drift-kinetic equation that MONKES solves and the transport coefficients that computes. In section 3 the algorithm to solve the drift-kinetic equation and its implementation are described. In section 4 we demonstrate that MONKES can be used to compute accurate monoenergetic coefficients at low collisionality in less than 2 minutes in a single processor for the $1/\nu$ and $\sqrt{\nu}$ regimes. These computations are also benchmarked against DKES and when necessary with the code SFINCS [26]. Finally, in section 5 we summarize the results and comment future lines of work and applications for MONKES.

2. Drift-kinetic equation and transport coefficients

The new code MONKES solves the drift-kinetic equation

$$(v\xi\boldsymbol{b} + \boldsymbol{v}_E) \cdot \nabla h_a + v\nabla \cdot \boldsymbol{b}\frac{(1-\xi^2)}{2}\frac{\partial h_a}{\partial \xi} - \nu^a \mathcal{L} h_a$$
$$= S_a, \quad (1)$$

where we have employed as velocity coordinates the cosine of the pitch-angle $\xi := \boldsymbol{v} \cdot \boldsymbol{b}/|\boldsymbol{v}|$ and the magnitude of the velocity $v := |\boldsymbol{v}|$, being $\boldsymbol{B}$ the magnetic field, $B := |\boldsymbol{B}|$ its strength and $\boldsymbol{b} = \boldsymbol{B}/B$ its unitary vector.

We assume that the magnetic configuration has nested flux surfaces. We denote by $\psi \in [0, \psi_{\text{lcfs}}]$ a radial coordinate that labels flux surfaces, where ψ_{lcfs} denotes the label of the last closed flux surface. In equation (1), h_a is the deviation of the distribution function from $f_{\text{M}a}w_{\text{M}a}$, where $f_{\text{M}a}$ is a local Maxwellian for a plasma species a

$$f_{\text{M}a}(\psi, v) = n_a(\psi)\pi^{-3/2}v_{ta}^{-3}(\psi)\exp\left(-\frac{v^2}{v_{ta}^2(\psi)}\right) \quad (2)$$

and $w_{\text{M}a}$ is the weighting factor

$$w_{\text{M}a} = \frac{e_a}{T_a}\int_0^l \left(\boldsymbol{E} \cdot \boldsymbol{B} - \langle \boldsymbol{E} \cdot \boldsymbol{B}\rangle\frac{B^2}{\langle B^2\rangle}\right)\frac{\mathrm{d}l'}{B}. \quad (3)$$

Here, n_a is the density of species a, $v_{ta} := \sqrt{2T_a/m_a}$ is its thermal velocity, T_a its temperature (in energy units), m_a its mass and e_a its charge. We denote the length along magnetic field lines by l, $\boldsymbol{E}$ is the electric field and the symbol $\langle...\rangle$ stands for the flux surface average operation. For the convective term in equation (1)

$$\boldsymbol{v}_E := \frac{\boldsymbol{E}_0 \times \boldsymbol{B}}{\langle B^2\rangle} = -E_\psi(\psi)\frac{\boldsymbol{B} \times \nabla\psi}{\langle B^2\rangle} \quad (4)$$

denotes the incompressible $\boldsymbol{E} \times \boldsymbol{B}$ drift approximation and $\boldsymbol{E}_0 = E_\psi(\psi)\nabla\psi$ is the piece of the electric field perpendicular to the flux surface. We denote the Lorentz pitch-angle scattering operator by

$$\mathcal{L} = \frac{1}{2}\frac{\partial}{\partial\xi}\left((1-\xi^2)\frac{\partial}{\partial\xi}\right). \quad (5)$$

In the collision operator, $\nu^a(v) = \sum_b \nu^{ab}(v)$ and

$$\nu^{ab}(v) := \frac{4\pi n_b e_a^2 e_b^2}{m_a^2 v_{ta}^3}\log\Lambda\frac{\mathrm{erf}(v/v_{tb}) - G(v/v_{tb})}{v^3/v_{ta}^3} \quad (6)$$

stands for the pitch-angle collision frequency between species a and b. We denote the Chandrasekhar function by $G(x) = \left[\mathrm{erf}(x) - (2x/\sqrt{\pi})\exp(-x^2)\right]/(2x^2)$, $\mathrm{erf}(x)$ is the error function and $\log\Lambda$ is the Coulomb logarithm [27].

On the right-hand-side of equation (1)

$$S_a := -\boldsymbol{v}_{\text{m}a} \cdot \nabla\psi\left(A_{1a} + \frac{v^2}{v_{ta}^2}A_{2a}\right)f_{\text{M}a} + Bv\xi A_{3a}f_{\text{M}a} \quad (7)$$

is the source term,

$$\boldsymbol{v}_{\text{m}a} \cdot \nabla\psi = -\frac{Bv^2}{\Omega_a}\frac{1+\xi^2}{2B^3}\boldsymbol{B} \times \nabla\psi \cdot \nabla B \quad (8)$$

is the expression of the radial magnetic drift assuming ideal magnetohydrodynamical equilibrium, $\Omega_a = e_a B/m_a$ is the gyrofrecuency and the flux functions

$$A_{1a}(\psi) := \frac{\mathrm{d}\ln n_a}{\mathrm{d}\psi} - \frac{3}{2}\frac{\mathrm{d}\ln T_a}{\mathrm{d}\psi} - \frac{e_a E_\psi}{T_a}, \quad (9)$$

$$A_{2a}(\psi) := \frac{\mathrm{d}\ln T_a}{\mathrm{d}\psi}, \quad (10)$$

$$A_{3a}(\psi) := \frac{e_a}{T_a}\frac{\langle \boldsymbol{E} \cdot \boldsymbol{B}\rangle}{\langle B^2\rangle}, \quad (11)$$

are the so-called thermodinamical forces.

The solution to equation (1) is determined up to an additive function $g(\psi, v)$. This function is

unimportant as it does not contribute to the transport coefficients. Nevertheless, in order to have a unique solution to the drift-kinetic equation, it must be fixed by imposing an appropriate additional constraint. We will select this free function (for fixed (ψ, v)) by imposing

$$\left\langle \int_{-1}^{1} h_a \, \mathrm{d}\xi \right\rangle = C, \qquad (12)$$

for some $C \in \mathbb{R}$ that will be determined indirectly.

The drift-kinetic equation (1) is the one presented in [28]. An equivalent form of this equation is solved by the standard neoclassical code DKES [25] using a variational principle.

Taking the moments $\{\boldsymbol{v}_{\mathrm{ma}} \cdot \nabla\psi, (v^2/v_{\mathrm{ta}}^2)\boldsymbol{v}_{\mathrm{ma}} \cdot \nabla\psi, v\xi B\}$ of h_a and then the flux-surface average yields, respectively, the radial particle flux, the radial heat flux and the parallel flow

$$\langle \boldsymbol{\Gamma}_a \cdot \nabla\psi \rangle := \left\langle \int \boldsymbol{v}_{\mathrm{ma}} \cdot \nabla\psi \; h_a \, \mathrm{d}^3\boldsymbol{v} \right\rangle, \qquad (13)$$

$$\left\langle \frac{\boldsymbol{Q}_a \cdot \nabla\psi}{T_a} \right\rangle := \left\langle \int \frac{v^2}{v_{\mathrm{ta}}^2} \boldsymbol{v}_{\mathrm{ma}} \cdot \nabla\psi \; h_a \, \mathrm{d}^3\boldsymbol{v} \right\rangle, \qquad (14)$$

$$\langle n_a \boldsymbol{V}_a \cdot \boldsymbol{B} \rangle := \left\langle B \int v\xi \; h_a \, \mathrm{d}^3\boldsymbol{v} \right\rangle. \qquad (15)$$

It is a common practice for linear drift-kinetic equations (e.g. [28], [29], [26]) to apply superposition and split h_a in three additive terms. Each one of them is a solution to the drift-kinetic equation using as source one of the three summands of the right hand side of definition (7). Besides, as in the drift-kinetic equation (1) there are no derivatives or integrals along ψ nor v, it is convenient to use the splitting

$$h_a = f_{\mathrm{Ma}} \left[\frac{Bv}{\Omega_a} \left(A_{1a} f_1 + A_{2a} \frac{v^2}{v_{\mathrm{ta}}^2} f_2 \right) + A_{3a} f_3 \right], \quad (16)$$

relating h_a to three functions $\{f_j\}_{j=1}^3$. The splitting is chosen so that the functions $\{f_j\}_{j=1}^3$ are solutions to

$$\xi \boldsymbol{b} \cdot \nabla f_j + \nabla \cdot \boldsymbol{b} \frac{(1-\xi^2)}{2} \frac{\partial f_j}{\partial \xi} - \frac{\hat{E}_\psi}{\langle B^2 \rangle} \boldsymbol{B} \times \nabla\psi \cdot \nabla f_j$$
$$- \hat{\nu}\mathcal{L}f_j = s_j, \qquad (17)$$

for $j = 1, 2, 3$, where $\hat{\nu} := \nu(v)/v$ and $\hat{E}_\psi := E_\psi/v$. The source terms are defined as

$$s_1 := -\boldsymbol{v}_{\mathrm{ma}} \cdot \nabla\psi \frac{\Omega_a}{Bv^2}, \quad s_2 := s_1, \quad s_3 := \xi B. \quad (18)$$

The relation between h_a and f_j given by equation (16) is such that the transport quantities (13), (14) and (15) can be written in terms of three transport coefficients which for fixed $(\hat{\nu}, \hat{E}_\psi)$ depend only on the magnetic configuration. As $\mathrm{d}\hat{\nu}/\mathrm{d}v$ never annuls,

the dependence of f_j on the velocity v can be parametrized by its dependence on $\hat{\nu}$. Thus, for fixed $(\hat{\nu}, \hat{E}_\psi)$, equation (17) is completely determined by the magnetic configuration. Hence, its unique solutions f_j that satisfy condition (12) are also completely determined by the magnetic configuration. The ad-hoc assumptions that lead to ψ and v appearing as mere parameters in the drift-kinetic equation (1) comprise the so called monoenergetic approximation to neoclassical transport (see e.g. [30]).

Using (16) we can write the transport quantities (13), (14) and (15) in terms of the Onsager matrix

$$\begin{bmatrix} \langle \boldsymbol{\Gamma}_a \cdot \nabla\psi \rangle \\ \left\langle \frac{\boldsymbol{Q}_a \cdot \nabla\psi}{T_a} \right\rangle \\ \langle n_a \boldsymbol{V}_a \cdot \boldsymbol{B} \rangle \end{bmatrix} = \begin{bmatrix} L_{11a} & L_{12a} & L_{13a} \\ L_{21a} & L_{22a} & L_{23a} \\ L_{31a} & L_{32a} & L_{33a} \end{bmatrix} \begin{bmatrix} A_{1a} \\ A_{2a} \\ A_{3a} \end{bmatrix}. \tag{19}$$

We have defined the thermal transport coefficients as

$$L_{ija} := \int_0^\infty 2\pi v^2 f_{\mathrm{Ma}} w_i w_j D_{ija} \, \mathrm{d}v, \qquad (20)$$

where $w_1 = w_3 = 1$, $w_2 = v^2/v_{\mathrm{ta}}^2$ and we have used that $\int g \, \mathrm{d}^3\boldsymbol{v} = 2\pi \int_0^\infty \int_{-1}^1 gv^2 \, \mathrm{d}\xi \, \mathrm{d}v$ for any integrable function $g(\xi, v)$. The quantities D_{ija} are the monoenergetic transport coefficients, defined as

$$D_{ija} := \frac{B^2 v^3}{\Omega_a^2} \widehat{D}_{ij}, \qquad i, j \in \{1, 2\}, \qquad (21)$$

$$D_{i3a} := \frac{Bv^2}{\Omega_a} \widehat{D}_{i3}, \qquad i \in \{1, 2\}, \qquad (22)$$

$$D_{3ja} := \frac{Bv^2}{\Omega_a} \widehat{D}_{3j}, \qquad j \in \{1, 2\}, \qquad (23)$$

$$D_{33a} := v\widehat{D}_{33}, \qquad (24)$$

and $\widehat{D}_{ij}$ are the monoenergetic geometric coefficients

$$\widehat{D}_{ij}(\psi, v) := \left\langle \int_{-1}^1 s_i f_j \, \mathrm{d}\xi \right\rangle, \quad i, j \in \{1, 2, 3\}. \quad (25)$$

Note that, unlike D_{ija}, the monoenergetic geometric coefficients $\widehat{D}_{ij}$ do not depend on the species for fixed $\hat{\nu}$ (however the correspondent value of v associated to each $\hat{\nu}$ varies between species) and depend only on the magnetic geometry. Of the monoenergetic geometric coefficients $\widehat{D}_{ij}$ only three of them are independent as Onsager symmetry implies $\widehat{D}_{13} = \widehat{D}_{31}$. Hence, obtaining the transport coefficients for all species requires to solve (17) for two different source terms s_1 and s_3. The algorithm for solving equation (17) is described in the next section.

3. Numerical method

In this section we describe the algorithm implemented to numerically solve the drift-kinetic equation (17). We

drop the subscript j from that labels every different source term. Also, as ψ and v act as mere parameters we will omit their dependence in this section and functions of these two variables will be referred as constants. First, in subsection 3.1 we will present the algorithm in a formal and abstract manner which is valid for any set of spatial coordinates. The algorithm, based on the tridiagonal representation of the drift-kinetic equation, merges naturally when discretizing the velocity coordinate ξ using a Legendre spectral method. Nevertheless, for convenience, we will explain it in (right-handed) Boozer coordinates $(\psi, \theta, \zeta) \in [0, \psi_{\text{lcfs}}] \times [0, 2\pi] \times [0, 2\pi/N_p]$. In these coordinates $2\pi\psi$ is the toroidal flux of the magnetic field and θ, ζ are respectively the poloidal and toroidal (in a single period) angles. The integer $N_p \geq 1$ denotes the number of periods of the device. In Boozer coordinates the magnetic field can be written as

$$\begin{aligned}\boldsymbol{B} &= \nabla\psi \times \nabla\theta - \iota(\psi)\nabla\psi \times \nabla\zeta \\ &= B_\psi(\psi,\theta,\zeta)\nabla\psi + B_\theta(\psi)\nabla\theta + B_\zeta(\psi)\nabla\zeta,\end{aligned} \quad (26)$$

and the Jacobian of the transformation reads

$$\sqrt{g}(\psi,\theta,\zeta) := (\nabla\psi \times \nabla\theta \cdot \nabla\zeta)^{-1} = \frac{B_\zeta + \iota B_\theta}{B^2}, \quad (27)$$

where $\iota := \boldsymbol{B} \cdot \nabla\theta/\boldsymbol{B} \cdot \nabla\zeta$ is the rotational transform. Using (26) and (27), the spatial differential operators present in the drift-kinetic equation (17) can be expressed in these coordinates as

$$\boldsymbol{b} \cdot \nabla = \frac{B}{B_\zeta + \iota B_\theta}\left(\iota\frac{\partial}{\partial\theta} + \frac{\partial}{\partial\zeta}\right), \quad (28)$$

$$\boldsymbol{B} \times \nabla\psi \cdot \nabla = \frac{B^2}{B_\zeta + \iota B_\theta}\left(B_\zeta\frac{\partial}{\partial\theta} - B_\theta\frac{\partial}{\partial\zeta}\right). \quad (29)$$

After the abstract explanation of the algorithm, in subsection 3.2 we explain how is implemented in MONKES.

3.1. Legendre polynomial expansion

The algorithm is based on the approximate representation of the distribution function f in a truncated Legendre series. We will search for approximate solutions to equation (17) of the form

$$f(\theta,\zeta,\xi) = \sum_{k=0}^{N_\xi} f^{(k)}(\theta,\zeta)P_k(\xi), \quad (30)$$

where $f^{(k)} = \langle f, P_k\rangle_{\mathcal{L}}/\langle P_k, P_k\rangle_{\mathcal{L}}$ is the k−th Legendre mode of $f(\theta,\zeta,\xi)$ (see Appendix A) and N_ξ is an integer greater or equal to 1. Of course, in general, the exact solution to equation (17) does not have a finite Legendre spectrum, but taking N_ξ sufficiently high in expansion (30) yields an approximate solution

to the desired degree of accuracy (in infinite precision arithmetic).

In Appendix A we derive explicitly the projection of each term of the drift-kinetic equation (17) onto the Legendre basis when the representation (30) is used. When doing so, we get that the Legendre modes of the drift-kinetic equation have the tridiagonal representation

$$L_k f^{(k-1)} + D_k f^{(k)} + U_k f^{(k+1)} = s^{(k)}, \quad (31)$$

for $k = 0, 1, \ldots, N_\xi$, where we have defined for convenience $f^{(-1)} := 0$ and from expansion (30) is clear that $f^{(N_\xi+1)} = 0$. Analogously to (30) the source term is expanded as $s = \sum_{k=0}^{N_\xi} s^{(k)}P_k$, and for the sources (18) this expansion is exact when $N_\xi \geq 2$. The spatial differential operators read

$$L_k = \frac{k}{2k-1}\left(\boldsymbol{b} \cdot \nabla + \frac{k-1}{2}\boldsymbol{b} \cdot \nabla\ln B\right), \quad (32)$$

$$D_k = -\frac{\hat{E}_\psi}{\langle B^2\rangle}\boldsymbol{B} \times \nabla\psi \cdot \nabla + \frac{k(k+1)}{2}\hat{\nu}, \quad (33)$$

$$U_k = \frac{k+1}{2k+3}\left(\boldsymbol{b} \cdot \nabla - \frac{k+2}{2}\boldsymbol{b} \cdot \nabla\ln B\right). \quad (34)$$

Thanks to its tridiagonal structure, the system of equations (31) can be formally inverted using the standard Gaussian elimination algorithm for block tridiagonal matrices. Before introducing the algorithm we will explain how to fix the free constant of the solution to equation (31) so that it can be inverted. Note that the aforementioned nullspace of the drift-kinetic equation translates in the fact that $f^{(0)}$ is not completely determined from equation (31). To prove this, we inspect the modes $k = 0$ and $k = 1$ that involve $f^{(0)}$. From expression (29) we can deduce that the term $D_0 f^{(0)} + U_0 f^{(1)}$ is invariant if we add to $f^{(0)}$ any function of $B_\theta(\psi)\zeta + B_\zeta(\psi)\theta$ when $\hat{E}_\psi \neq 0$ and does not include $f^{(0)}$ for $\hat{E}_\psi = 0$. Besides, the term $L_1 f^{(0)} + D_1 f^{(1)} + U_1 f^{(2)}$ remains invariant if we add to $f^{(0)}$ any constant. Thus, equation (31) is unaltered when we add to $f^{(0)}$ a constant. A constraint equivalent to condition (12) is to fix the value of the 0−th Legendre mode of the distribution function at a single point of the flux-surface. For example,

$$f^{(0)}(0,0) = 0. \quad (35)$$

With this condition, equation (31) has a unique solution and can be inverted (further details on its invertibility are given in Appendix B) to obtain an approximation of the first $N_\xi + 1$ Legendre modes of the solution to the drift-kinetic equation (17).

The algorithm for formally solving the truncated drift-kinetic equation (31) consists of two steps.

(i) **Forward elimination**

Starting from $\Delta_{N_\xi} = D_{N_\xi}$ and $\sigma^{(N_\xi)} = s^{(N_\xi)}$ we can obtain recursively the operators

$$\Delta_k = D_k - U_k \Delta_{k+1}^{-1} L_{k+1}, \tag{36}$$

and the sources

$$\sigma^{(k)} = s^{(k)} - U_k \Delta_{k+1}^{-1} \sigma^{(k+1)}, \tag{37}$$

for $k = N_\xi - 1, N_\xi - 2, \ldots, 0$ (in this order). Equations (36) and (37) define the forward elimination. With this procedure we can transform equation (31) to the equivalent system

$$L_k f^{(k-1)} + \Delta_k f^{(k)} = \sigma^{(k)}, \tag{38}$$

for $k = 0, 1, \ldots, N_\xi$. Note that this process corresponds to perform formal Gaussian elimination over

$$\left[\begin{array}{ccc|c} L_k & D_k & U_k & s^{(k)} \\ 0 & L_{k+1} & \Delta_{k+1} & \sigma^{(k+1)} \end{array} \right], \tag{39}$$

to eliminate U_k in the first row.

(ii) **Backward substitution**

Once we have the system of equations in the form (38) it is immediate to solve recursively

$$f^{(k)} = \Delta_k^{-1} \left(\sigma^{(k)} - L_k f^{(k-1)} \right), \tag{40}$$

for $k = 0, 1, ..., N_\xi$ (in this order). Here, we denote by $\Delta_0^{-1} \sigma^{(0)}$ to the solution that satisfies (35). We recall that for $k = 0$, we must impose condition (35) so that $\Delta_0 f^{(0)} = \sigma^{(0)}$ has a unique solution. As $L_1 = \boldsymbol{b} \cdot \nabla$, using expression (28), it is apparent from equation (40) that the integration constant does not affect the value of $f^{(1)}$.

We can apply this algorithm to solve equation (17) for f_1, f_2 and f_3 in order to compute approximations to the transport coefficients. In terms of the Legendre modes of f_1, f_2 and f_3, the monoenergetic geometric coefficients from definition (25) read

$$\widehat{D}_{11} = 2 \left\langle s_1^{(0)} f_1^{(0)} \right\rangle + \frac{2}{5} \left\langle s_1^{(2)} f_1^{(2)} \right\rangle, \tag{41}$$

$$\widehat{D}_{31} = \frac{2}{3} \left\langle B f_1^{(1)} \right\rangle, \tag{42}$$

$$\widehat{D}_{13} = 2 \left\langle s_1^{(0)} f_3^{(0)} \right\rangle + \frac{2}{5} \left\langle s_1^{(2)} f_3^{(2)} \right\rangle, \tag{43}$$

$$\widehat{D}_{33} = \frac{2}{3} \left\langle B f_3^{(1)} \right\rangle, \tag{44}$$

where $3s_1^{(0)}/2 = 3s_1^{(2)} = \boldsymbol{B} \times \nabla\psi \cdot \nabla B / B^3$. Note that, in order to compute the monoenergetic geometric coefficients $\widehat{D}_{ij}$ from expressions (41), (42), (43) and (44), we only need to calculate the Legendre modes $k = 0, 1, 2$ of the solution and we can stop the backward substitution (40) at $k = 2$. In the next subsection we will explain how MONKES approximately solves equation (31) using this algorithm.

3.2. Spatial discretization and algorithm implementation

The algorithm described above allows, in principle, to compute the exact solution to the truncated drift-kinetic equation (31) which is an approximate solution to (17). However, it is not possible, to our knowledge, to give an exact expression for the operator Δ_k^{-1} except for $k = N_\xi \geq 1$. Instead, we are forced to compute an approximate solution to (31). In order to obtain an approximate solution of equation (31) we assume that each $f^{(k)}$ has a finite Fourier spectrum so that it can be expressed as

$$f^{(k)}(\theta, \zeta) = \boldsymbol{I}(\theta, \zeta) \cdot \boldsymbol{f}^{(k)}, \tag{45}$$

where the Fourier interpolant row vector map $\boldsymbol{I}(\theta, \zeta)$ is defined at Appendix C and the column vector $\boldsymbol{f}^{(k)} \in \mathbb{R}^{N_{\text{fs}}}$ contains $f^{(k)}$ evaluated at the equispaced grid points

$$\theta_i = 2\pi i / N_\theta, \qquad i = 0, 1, \ldots, N_\theta - 1, \tag{46}$$

$$\zeta_j = 2\pi j / (N_\zeta N_p), \qquad j = 0, 1, \ldots, N_\zeta - 1. \tag{47}$$

Here, $N_{\text{fs}} := N_\theta N_\zeta$ is the number of points in which we discretize the flux surface being N_θ and N_ζ respectively the number of points in which we divide θ and ζ. The exact solution to equation (31) in general has an infinite Fourier spectrum and cannot exactly be written as (45), but taking N_θ and N_ζ sufficiently big, we can approximate the solution to equation (31) to arbitrary degree of accuracy (in infinite precision arithmetic). As is explained in Appendix C, introducing the Fourier interpolant (45) in equation (31) and then evaluating the result at the grid points, we obtain a system of $N_{\text{fs}} \times (N_\xi + 1)$ equations which can be solved for $\{\boldsymbol{f}^{(k)}\}_{k=0}^{N_\xi}$. This system of equations is obtained by substituting the operators L_k, D_k, U_k in equation (31) by the $N_{\text{fs}} \times N_{\text{fs}}$ matrices $\boldsymbol{L}_k, \boldsymbol{D}_k, \boldsymbol{U}_k$, defined in Appendix C. Thus, we discretize (31) as

$$\boldsymbol{L}_k \boldsymbol{f}^{(k-1)} + \boldsymbol{D}_k \boldsymbol{f}^{(k)} + \boldsymbol{U}_k \boldsymbol{f}^{(k+1)} = \boldsymbol{s}^{(k)}, \tag{48}$$

for $k = 0, 1 \ldots, N_\xi$. Obviously, this system has a block tridiagonal structure and the algorithm presented in subsection 3.1 can be applied to it. We just have to replace in equations (36), (37) and (40) the operators and functions by their matrix and vector analogues respectively. We will denote such matrix and vector analogues by boldface letters. The matrix approximation to the forward elimination procedure given by equations (36) and (37) reads

$$\boldsymbol{\Delta}_k = \boldsymbol{D}_k - \boldsymbol{U}_k \boldsymbol{\Delta}_{k+1}^{-1} \boldsymbol{L}_{k+1}, \tag{49}$$

$$\boldsymbol{\sigma}^{(k)} = \boldsymbol{s}^{(k)} - \boldsymbol{U}_k \boldsymbol{\Delta}_{k+1}^{-1} \boldsymbol{\sigma}^{(k+1)}, \tag{50}$$

for $k = N_\xi - 1, N_\xi - 2, \ldots, 0$ (in this order). Thus, starting from $\boldsymbol{\Delta}_{N_\xi} = \boldsymbol{D}_{N_\xi}$ and $\boldsymbol{\sigma}^{(N_\xi)} = \boldsymbol{s}^{(N_\xi)}$ all

the matrices $\boldsymbol{\Delta}_k$ and the vectors $\boldsymbol{\sigma}^{(k)}$ are defined from equations (49) and (50). Obtaining the matrix $\boldsymbol{\Delta}_k$ from equation (49) requires to invert $\boldsymbol{\Delta}_{k+1}$, perform two matrix multiplications and a subtraction of matrices. The inversion using LU factorization and each matrix multiplication require $O(N_{\text{fs}}^3)$ operations so it is desirable to reduce the number of matrix multiplications to one. For $k \geq 2$, we can reduce the number of matrix multiplications in determining $\boldsymbol{\Delta}_k$ to one if instead of computing $\boldsymbol{\Delta}_{k+1}^{-1}$ we solve for $\boldsymbol{X}_{k+1}$ the matrix system of equations

$$\boldsymbol{\Delta}_{k+1}\boldsymbol{X}_{k+1} = \boldsymbol{L}_{k+1}, \tag{51}$$

and then obtain

$$\boldsymbol{\Delta}_k = \boldsymbol{D}_k - \boldsymbol{U}_k\boldsymbol{X}_{k+1}, \tag{52}$$

for $k = N_\xi - 1, N_\xi - 2, \ldots, 2$. For $k \leq 1$ as we need to solve (38) and do the backward substitution (40), it is convenient to compute and store $\boldsymbol{\Delta}_k^{-1}$. Besides, as none of the source terms s_1, s_2 and s_3 given by (18) have Legendre modes greater than 2 we have from equation (50) that $\boldsymbol{\sigma}^{(k)} = 0$ for $k \geq 3$ and $\boldsymbol{\sigma}^{(2)} = \boldsymbol{s}^{(2)}$ and (50) must be applied just when $k = 0$ and $k = 1$. Applying once (50) requires $O(N_{\text{fs}}^2)$ operations and its contribution to the arithmetic complexity of the algorithm is subdominant with respect to the matrix inversions and multiplications. As the resolution of a matrix system of equations and matrix multiplication must be done $N_\xi + 1$ times, numerically solving equation (48) by this method requires $O(N_\xi N_{\text{fs}}^3)$ operations. In what concerns to memory resources, as we are only interested in the Legendre modes 0, 1 and 2, it is not necessary to store in memory all the matrices $\boldsymbol{L}_k$, $\boldsymbol{D}_k$, $\boldsymbol{U}_k$ and $\boldsymbol{\Delta}_k$. Instead, we store solely $\boldsymbol{L}_k$, $\boldsymbol{U}_k$ and $\boldsymbol{\Delta}_k^{-1}$ for $k = 0, 1, 2$. For the intermediate steps we just need to use some auxiliary matrices $\boldsymbol{L}$, $\boldsymbol{D}$, $\boldsymbol{U}$, $\boldsymbol{\Delta}$ and $\boldsymbol{X}$.

To summarize, the pseudocode of the implementation of the algorithm in `MONKES` is given in Algorithm 1. In the first loop from $k = N_\xi - 1$ to $k = 2$ we construct $\boldsymbol{L}_2$, $\boldsymbol{\Delta}_2^{-1}$ and $\boldsymbol{U}_2$ without saving any matrix from the intermediate steps nor computing any vector $\boldsymbol{\sigma}^{(k)}$. After that, in the second loop from $k = 1$ to $k = 0$, the matrices $\boldsymbol{L}_k$ and $\boldsymbol{\Delta}_k^{-1}$ are computed and saved for the posterior step of backward substitution.

Once we have solved (48) for $\boldsymbol{f}^{(0)}$, $\boldsymbol{f}^{(1)}$ and $\boldsymbol{f}^{(2)}$, the integrals of the flux surface average operation involved in the geometric coefficients (41), (42), (43) and (44), are conveniently computed using the trapezoidal rule, which for periodic analytic functions has geometric convergence [31]. In the next sections we will see that despite the cubic scaling in N_{fs} of the arithmetical complexity of the algorithm, it is possible to obtain fast and accurate calculations of the monoenergetic geometric coefficients at low

---

Algorithm 1 Block tridiagonal solution algorithm implemented in `MONKES`.

Forward elimination:

$\quad \boldsymbol{L} \leftarrow \boldsymbol{L}_{N_\xi}$ $\qquad\qquad\quad$ ▷ Starting value for $\boldsymbol{L}$
$\quad \boldsymbol{\Delta} \leftarrow \boldsymbol{D}_{N_\xi}$ $\qquad\qquad\quad$ ▷ Starting value for $\boldsymbol{\Delta}$
$\quad$ **for** $k = N_\xi - 1$ **to** 2 **do**
$\qquad$ Solve $\boldsymbol{\Delta}\boldsymbol{X} = \boldsymbol{L}$ $\quad$ ▷ Compute $\boldsymbol{X}_{k+1}$ stored in $\boldsymbol{X}$
$\qquad \boldsymbol{L} \leftarrow \boldsymbol{L}_k$ $\qquad\qquad$ ▷ Construct $\boldsymbol{L}_k$ stored in $\boldsymbol{L}$
$\qquad \boldsymbol{D} \leftarrow \boldsymbol{D}_k$ $\qquad\qquad$ ▷ Construct $\boldsymbol{D}_k$ stored in $\boldsymbol{D}$
$\qquad \boldsymbol{U} \leftarrow \boldsymbol{U}_k$ $\qquad\qquad$ ▷ Construct $\boldsymbol{U}_k$ stored in $\boldsymbol{U}$
$\qquad \boldsymbol{\Delta} \leftarrow \boldsymbol{D} - \boldsymbol{U}\boldsymbol{X}$ $\qquad$ ▷ Construct $\boldsymbol{\Delta}_k$ stored in $\boldsymbol{\Delta}$
$\qquad$ **if** $k = 2$ **then** $\qquad\qquad$ ▷ Save required matrices
$\qquad\qquad \boldsymbol{L}_k \leftarrow \boldsymbol{L}$ $\qquad\qquad\qquad\qquad$ ▷ Save $\boldsymbol{L}_2$
$\qquad\qquad$ Solve $\boldsymbol{\Delta}\boldsymbol{\Delta}_k^{-1} = $ Identity $\qquad$ ▷ Compute $\boldsymbol{\Delta}_2^{-1}$
$\qquad\qquad \boldsymbol{U}_k \leftarrow \boldsymbol{U}$ $\qquad\qquad\qquad\qquad$ ▷ Save $\boldsymbol{U}_2$
$\qquad$ **end if**
$\quad$ **end for**
$\quad$ **for** $k = 1$ **to** 0 **do**
$\qquad$ **if** $k > 0$ $\boldsymbol{L}_k \leftarrow \boldsymbol{L}_k$ $\qquad$ ▷ Construct and save $\boldsymbol{L}_k$
$\qquad \boldsymbol{D} \leftarrow \boldsymbol{D}_k$ $\qquad\qquad$ ▷ Construct $\boldsymbol{D}_k$ stored in $\boldsymbol{D}$
$\qquad \boldsymbol{U}_k \leftarrow \boldsymbol{U}_k$ $\qquad\qquad\qquad$ ▷ Construct and save $\boldsymbol{U}_k$
$\qquad \boldsymbol{\Delta}_k^{-1} \leftarrow \boldsymbol{D} - \boldsymbol{U}_k\boldsymbol{\Delta}_{k+1}^{-1}\boldsymbol{L}_k$ $\qquad$ ▷ Construct $\boldsymbol{\Delta}_k$
$\qquad \boldsymbol{\sigma}^{(k)} \leftarrow \boldsymbol{s}^{(k)} - \boldsymbol{U}_k\boldsymbol{\Delta}_{k+1}^{-1}\boldsymbol{\sigma}^{(k+1)}$ ▷ Construct $\boldsymbol{\sigma}^{(k)}$
$\qquad$ Solve $\boldsymbol{\Delta}\boldsymbol{\Delta}_k^{-1} = $ Identity $\qquad$ ▷ Compute $\boldsymbol{\Delta}_k^{-1}$
$\quad$ **end for**

Backward substitution:

$\quad \boldsymbol{f}^{(0)} \leftarrow \boldsymbol{\Delta}_0^{-1}\boldsymbol{\sigma}^{(0)}$
$\quad$ **for** $k = 1$ **to** 2 **do**
$\qquad \boldsymbol{f}^{(k)} \leftarrow \boldsymbol{\Delta}_k^{-1}\left(\boldsymbol{\sigma}^{(k)} - \boldsymbol{L}_k\boldsymbol{f}^{(k-1)}\right)$
$\quad$ **end for**

---

collisionality (in particular $\widehat{D}_{31}$) in a single processor. The reason behind this is that in the asymptotic relation $O(N_{\text{fs}}^3) \sim C_{\text{alg}}N_{\text{fs}}^3$, the constant C_{alg} is small enough to allow N_{fs} to take a value sufficiently high to capture accurately the spatial dependence of the distribution function without increasing much the wall-clock time. The algorithm is implemented in the new code `MONKES`, written in Fortran language. The matrix inversions and multiplications are computed using the linear algebra library `LAPACK` [32].

4. Numerical results and benchmark

At the low collisionality regime, convection is dominant with respect to diffusion and the solution to equation (17) posses boundary layers in ξ. These boundary layers appear at the interfaces between different classes of trapped particle. At these regions of phase space, collisions are no longer subdominant with respect to the advection. Also at these regions, the poloidal $\boldsymbol{E} \times \boldsymbol{B}$ precession from equation (17) can produce the chaotic transition of collisionless particles from one

class to another due to separatrix crossing mechanisms [33]. The existence of these localized regions with large ξ gradients forces to take a truncated expansion with a high number of Legendre modes N_ξ, making difficult to obtain fast and accurate solutions to equation (17). In this section we will demonstrate how MONKES provides fast and accurate calculations of the monoenergetic coefficients from low ($\hat{\nu} = 10^{-5}$ m^{-1}) to high collisionality ($\hat{\nu} = 3 \cdot 10^2$ m^{-1}) benchmarked with DKES and for some cases in which DKES calculations are not accurate, also with SFINCS.

Before proceeding, for the sake of clarity, we will translate the monoenergetic geometric coefficients defined by (25) to match the normalization of DKES output. First, the quantity $\hat{\nu}$ is called CMUL in the code DKES. For the electric field, $\hat{E}_\psi$ is related to the variable EFIELD from DKES via EFIELD $= \hat{E}_\psi \, \mathrm{d}\psi/\mathrm{d}r$ where $r^2/L_a^2 = \psi/\psi_{\text{lcfs}}$ and L_a is the minor radius of the device. We will denote by $\hat{E}_r := \hat{E}_\psi \, \mathrm{d}\psi/\mathrm{d}r$ to this quantity. The code DKES gives an approximation to the monoenergetic geometric coefficients as a semisum of two quantities $\widehat{D}_{ij}^-$ and $\widehat{D}_{ij}^+$ by solving a variational principle [25]. For each coefficient, the output of DKES consists on two columns containing $\widehat{D}_{ij}^\mp K_{ij}$, where K_{ij} are the normalization factors

$$K_{ij} := \left(\frac{\mathrm{d}\psi}{\mathrm{d}r}\right)^{-2}, \qquad i,j \in \{1,2\}, \qquad (53)$$

$$K_{i3} := -\left(\frac{\mathrm{d}\psi}{\mathrm{d}r}B_{00}\right)^{-1}, \qquad i \in \{1,2\}, \qquad (54)$$

$$K_{3j} := \left(\frac{\mathrm{d}\psi}{\mathrm{d}r}B_{00}\right)^{-1}, \qquad j \in \{1,2\}, \qquad (55)$$

$$K_{33} := -B_{00}^{-2}, \qquad (56)$$

where $B_{00} = N_p(2\pi)^{-2} \oint \oint B \, \mathrm{d}\theta \, \mathrm{d}\zeta$ is the $(0,0)$ Fourier mode of B. There is still a nuance left for the parallel conductivity coefficient: the code DKES computes this coefficient measured with respect to the one obtained by solving the Spitzer problem

$$-\hat{\nu}\mathcal{L}f_{\text{Sp}} = s_3. \qquad (57)$$

Using (A.1) is immediate to obtain the $1-$th Legendre mode of f_{Sp}

$$f_{\text{Sp}}^{(1)} = \frac{B}{\hat{\nu}} \qquad (58)$$

and using (44) we obtain its associated $\widehat{D}_{33}$ coefficient

$$\widehat{D}_{33,\text{Sp}} = \frac{2}{3\hat{\nu}}\langle B^2 \rangle. \qquad (59)$$

Thus, the output columns of DKES for the parallel conductivity coefficient $\widehat{D}_{33}^\mp K_{33}$ have to be compared against $(\widehat{D}_{33} - \widehat{D}_{33,\text{Sp}})K_{33}$. For the rest of the

Configuration	ψ/ψ_{lcfs}	$\hat{\nu}$ [m^{-1}]	$\hat{E}_r$ [kV$\cdot$s/m^2]
CIEMAT-QI	0.250	10^{-5}	0
CIEMAT-QI	0.250	10^{-5}	10^{-3}
W7X-EIM	0.200	10^{-5}	0
W7X-EIM	0.200	10^{-5}	$3 \cdot 10^{-4}$
W7X-KJM	0.204	10^{-5}	0
W7X-KJM	0.204	10^{-5}	$3 \cdot 10^{-4}$

Table 1: Cases considered to study the convergence of monoenergetic coefficients and values of $(\hat{\nu}, \hat{E}_r)$.

coefficients the output columns $\widehat{D}_{ij}^\mp K_{ij}$ of DKES are normalized in the same way as $\widehat{D}_{ij}K_{ij}$.

Finally, we inform that all the calculations shown are computed in a single core of one of the partitions of CIEMAT's cluster XULA. Specifically, in partition number 2‡ whose nodes run with Intel Xeon Gold 6254 cores which run at 3.10 GHz.

4.1. Convergence of monoenergetic coefficients at low collisionality

In this subsection we will demonstrate how the monoenergetic coefficients computed by MONKES converge with N_θ, N_ζ and N_ξ at low collsionality for three different magnetic configurations at a single flux surface. Two of them correspond to two modes of operation of W7-X: W7-X EIM (also called standard), W7-KJM (also called high mirror). The third one corresponds to the new QI "flat mirror" configuration CIEMAT-QI [9]. The calculations are for the $1/\nu$ ($\hat{E}_r = 0$) and $\sqrt{\nu}$ regimes at the low collisionality value $\hat{\nu} = 10^{-5}$. In table 1 the list of cases considered is enlisted with their correspondent values of $\hat{E}_r$.

For each configuration we will proceed in the same manner. First, we plot the (spatially converged) coefficients $\widehat{D}_{ij}$ as functions of the number of Legendre modes in a sufficiently wide interval. From the curve of $\widehat{D}_{31}$ vs N_ξ we define our converged reference value, which we denote by $\widehat{D}_{31}^{\text{r}}$, as the (spatially converged) calculation for the highest number of Legendre modes. From this converged reference value we define a region $\mathcal{R}_\epsilon := [(1 - \epsilon/100)\widehat{D}_{31}^{\text{r}}, (1 + \epsilon/100)\widehat{D}_{31}^{\text{r}}]$ of calculations that deviate less than or equal to an $\epsilon\%$ with respect to $\widehat{D}_{31}^{\text{r}}$. Now we can define properly what it means to be "sufficiently converged". We say that, for fixed $(N_\theta, N_\zeta, N_\xi)$ and ϵ, a calculation $\widehat{D}_{31} \in \mathcal{R}_\epsilon$ is sufficiently converged if, two conditions are satisfied

(i) Spatially converged calculations with $N_\xi' > N_\xi$ still belong to $\mathcal{R}_\epsilon$.

‡ Partition number 1 whose nodes use Intel Xeon Gold 6148 cores which run at 2.4 GHz. Typically it has been found that this partition is 1.1-1.2 times faster. Nevertheless, in order to be conservative, we show MONKES results on the slower cores.
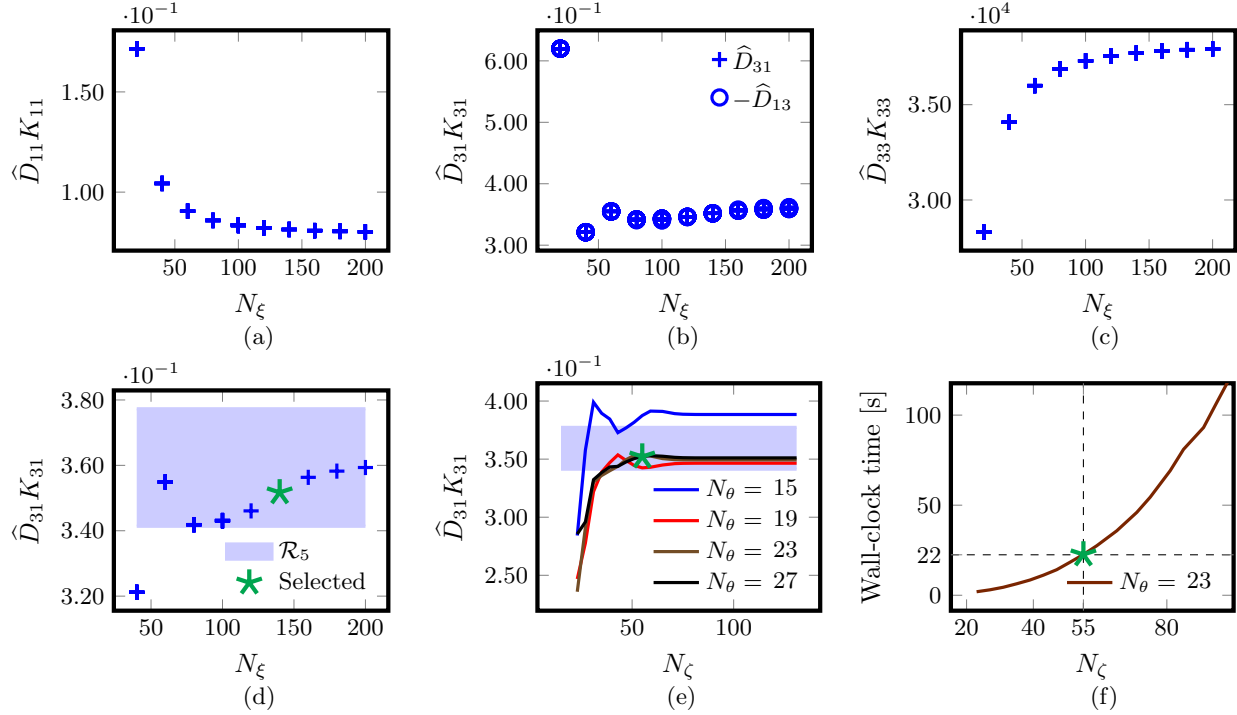
Figure 1: Convergence of monoenergetic coefficients with the number of Legendre modes N_ξ for W7X-EIM at the surface labelled by $\psi/\psi_{\text{lcfs}} = 0.200$, for $\hat{\nu}(v) = 10^{-5}$ m^{-1} and $\hat{E}_r(v) = 0$ kV $\cdot$ s/m^2.

(ii) Increasing N_θ and N_ζ keeping N_ξ constant produces calculations which belong to $\mathcal{R}_\epsilon$.

Condition (i) is used to select the number of Legendre modes N_ξ and condition (ii) is used to select the values of N_θ and N_ζ once N_ξ is fixed.

On figure 1 the convergence of monoenergetic coefficients with the number of Legendre modes is shown for W7-X EIM in the $1/\nu$ regime. It is also shown that the bootstrap current and Ware pinch coefficients are the most difficult to converge. From figure 1b we can check that the calculation for $N_\xi = 200$ can be safely considered as our converged reference value $\widehat{D}_{31}^{\text{r}}$. We choose the value of $\epsilon = 5\%$ to define $\mathcal{R}_5$ as shown in figure 1d. We conclude from this figure that any value of $N_\xi \geq 80$ satisfies condition (i) of our definition of sufficiently converged. In order to not to be too indulgent with MONKES calculations we select $N_\xi = 140$ as indicated by the green five-point star§. As shown in figures 1e and 1f the values $(N_\theta, N_\zeta) = (23, 55)$ satisfy condition (ii). On figure 1f we plot the wall-clock time spent in MONKES calculations of the monoenergetic coefficients for our selection $(N_\theta, N_\xi) = (23, 140)$ as a function of N_ζ. With a green star, we indicate the wall-clock time spent by our selection of resolutions, which is of 22 seconds.

§ Being strict with our definition we could take half these number of Legendre modes and still obtain a sufficiently converged calculation.

In practice, it might not be possible to carry out a convergence study every time MONKES is going to be used, i.e. it is not possible to check that our calculation satisfies convergence conditions (i) and (ii). Hence, for each case we will provide a list of alternative possibilities to illustrate that many selections yield fast and accurate results. On table 2 we display some other selections of the triplet $(N_\theta, N_\zeta, N_\xi)$ that provide fast and accurate calculations of the $\widehat{D}_{31}$ coefficient. All these triplets are selected so that they lie on our defined region of convergence $\mathcal{R}_5$ and are computed in less than 120 seconds.

For the $\sqrt{\nu}$ regime case of W7-X EIM on figure 2b we check again that the calculation for $N_\xi = 200$ serves as a good converged reference value $\widehat{D}_{31}^{\text{r}}$. On figure 2d we notice that to obtain sufficiently converged results for the region $\mathcal{R}_5$ is more difficult than in the previous $1/\nu$ regime. This is in part due to the fact that the $\widehat{D}_{31}$ coefficient is smaller in absolute value and thus, the region $\mathcal{R}_5$ is narrower. Inspecting this plot, with the same spirit as before of not trying to be too indulgent, we select $N_\xi = 160$ (green star) to satisfy condition (i). The selection $(N_\theta, N_\zeta) = (27, 55)$ satisfies condition (ii) as shown in figure 2e. From figure 2f we check that it required 40 seconds to compute the monoenergetic coefficients with this selection of $(N_\theta, N_\zeta, N_\xi)$, which is quite fast. More triplets that give fast and accurate calculations of the $\widehat{D}_{31}$ coefficient are given on table 3.
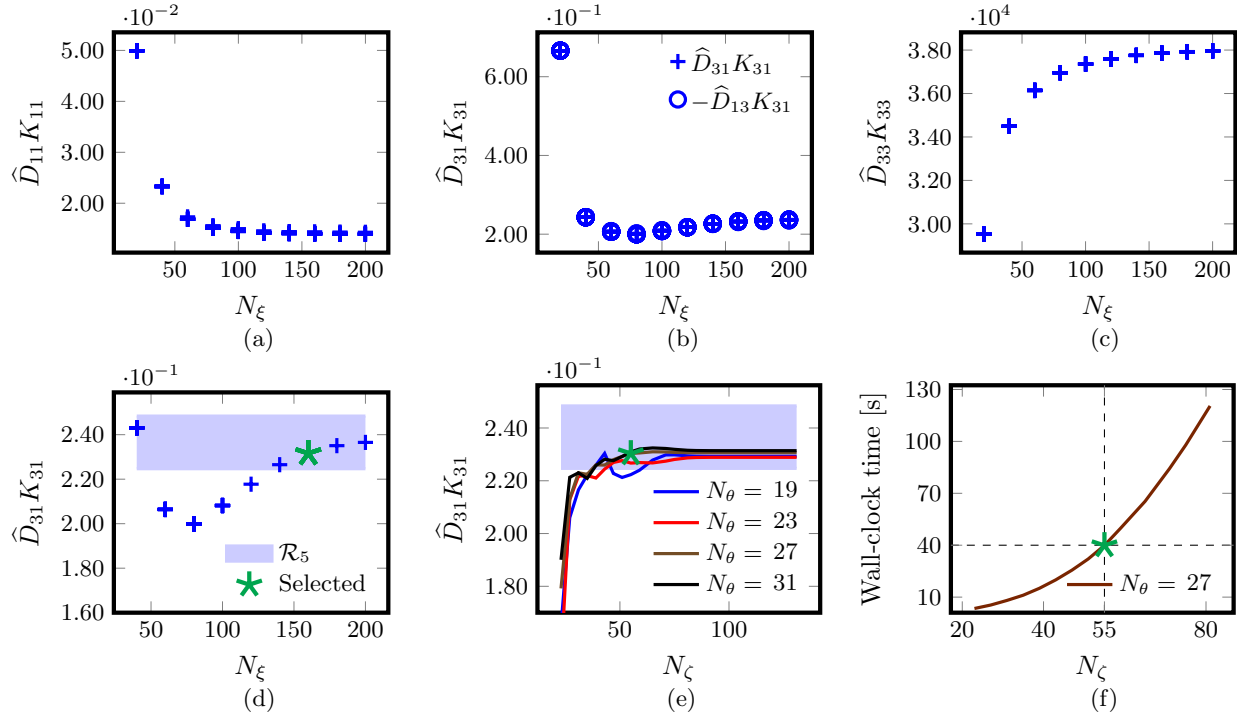
Figure 2: Convergence of monoenergetic coefficients with the number of Legendre modes N_ξ for W7X-EIM at the surface labelled by $\psi/\psi_{\mathrm{lcfs}} = 0.200$, for $\hat{\nu}(v) = 10^{-5}$ m^{-1} and $\hat{E}_r = 3 \cdot 10^{-4}$ kV $\cdot$ s/m^2.

N_θ	N_ζ	N_ξ	t_{clock} [s]
21	75	{100, 120, 140, 160, 180, 200, 220, 240, 260}	{31, 37, 43, 49, 55, 61, 67, 73, 79}
21	99	{100, 120, 140, 160, 180}	{66, 79, 92, 105, 118}
23	75	{100, 120, 140, 160, 180, 200, 220, 240, 260}	{40, 47, 55, 63, 70, 78, 86, 94, 102}
27	75	{100, 120, 140, 160, 180}	{61, 73, 85, 97, 109}
27	85	{100, 120}	{87, 105}

Table 2: Additional triplets $(N_\theta, N_\zeta, N_\xi)$ that give a fast and accurate calculation of $\widehat{D}_{31}$ for W7X-EIM at the surface labelled by $\psi/\psi_{\mathrm{lcfs}} = 0.200$, for $\hat{\nu}(v) = 10^{-5}$ m^{-1} and $\hat{E}_r(v) = 0$ kV $\cdot$ s/m^2.

N_θ	N_ζ	N_ξ	t_{clock} [s]
21	75	{160, 180, 200, 220, 240, 260, 280, 300, 320}	{49, 55, 61, 67, 73, 79 85,91,97}
21	99	{160, 180}	{105, 118}
23	75	{160, 180, 200, 220, 240, 260 280, 300}	{63, 70, 78, 86, 94, 102 109, 117 }
31	51	{140, 160, 180, 200, 220, 240, 260, 280, 300}	{43, 50, 56, 62, 68, 74, 80, 86, 92}

Table 3: Additional triplets $(N_\theta, N_\zeta, N_\xi)$ that give a fast and accurate calculation of $\widehat{D}_{31}$ for W7X-EIM at the surface labelled by $\psi/\psi_{\mathrm{lcfs}} = 0.200$, for $\hat{\nu}(v) = 10^{-5}$ m^{-1} and $\hat{E}_r(v) = 3 \cdot 10^{-4}$ kV $\cdot$ s/m^2.

For the high mirror configuration of W7-X in the $1/\nu$ we can use again the calculation for $N_\xi = 200$ as the converged reference value $\widehat{D}_{31}^{\mathrm{r}}$ as shown in figure 3b. Due to the smaller value of $\widehat{D}_{31}^{\mathrm{r}}$ the amplitude of the region $\mathcal{R}_5$ is much narrower, being of order 10^{-3}. On figure 3d we see that taking $N_\xi = 140$ is sufficient to satisfy convergence condition (i). According to the convergence curves shown in figure 3e, taking

$(N_\theta, N_\zeta) = (23, 63)$ would yield a calculation that satisfies condition (ii). This calculation is also quite fast as can be checked from figure 3f, with a wall-clock time of 33 seconds. Again, we display other possible selections that lie on $\mathcal{R}_5$ on table 4.
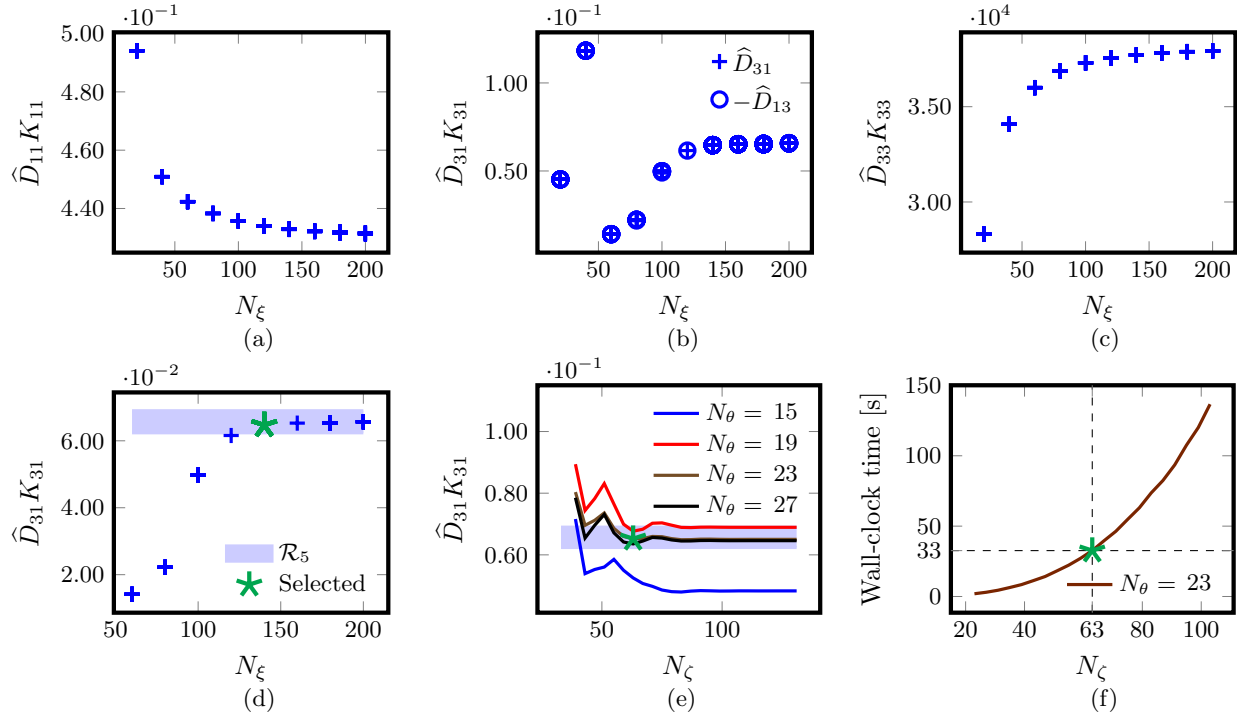
Figure 3: Convergence of monoenergetic coefficients with the number of Legendre modes N_ξ for W7X-KJM at the surface labelled by $\psi/\psi_{\text{lcfs}} = 0.204$, for $\hat{\nu}(v) = 10^{-5}$ m^{-1} and $\hat{E}_r(v) = 0$ kV $\cdot$ s/m^2.

N_θ	N_ζ	N_ξ	t_{clock} [s]
21	75	$\{140, 160, 180\}$	$\{43, 49, 55\}$
21	99	$\{140, 160, 180\}$	$\{92, 105, 118\}$
23	75	$\{140, 160\}$	$\{84, 96\}$
27	75	$\{140, 160, 180\}$	$\{87, 99, 111\}$

Table 4: Additional triplets $(N_\theta, N_\zeta, N_\xi)$ that give a fast and accurate calculation of $\widehat{D}_{31}$ for W7X-KJM at the surface labelled by $\psi/\psi_{\text{lcfs}} = 0.204$, for $\hat{\nu}(v) = 10^{-5}$ m^{-1} and $\hat{E}_r(v) = 0$ kV $\cdot$ s/m^2.

N_θ	N_ζ	N_ξ	t_{clock} [s]
19	75	$\{140, 160, 180,$ $200, 220, 240,$ $260, 280, 300\}$	$\{48, 55, 62,$ $69, 75, 82,$ $89, 96, 103\}$
21	75	$\{140, 160, 180,$ $200, 220, 240,$ $260, 280, 300\}$	$\{43, 49, 55,$ $61, 67, 73,$ $80, 86, 91\}$
21	99	$\{140, 160, 180\}$	$\{92, 105, 118\}$
23	75	$\{140, 160, 180\}$	$\{84, 96, 108\}$
31	51	$\{160, 180, 200,$ $220, 240\}$	$\{76, 86, 95,$ $105, 114\}$

Table 5: Additional triplets $(N_\theta, N_\zeta, N_\xi)$ that give a fast and accurate calculation of $\widehat{D}_{31}$ for W7X-KJM at the surface labelled by $\psi/\psi_{\text{lcfs}} = 0.200$, for $\hat{\nu}(v) = 10^{-5}$ m^{-1} and $\hat{E}_r(v) = 3 \cdot 10^{-4}$ kV $\cdot$ s/m^2.

For the high mirror configuration of W7-X in the $\sqrt{\nu}$ the (spatially converged) calculation for $N_\xi = 200$ serves as the converged reference value $\widehat{D}_{31}^{\text{r}}$ as can be checked in figure 3b. The selection of Legendre modes $N_\xi = 140$ to have a calculation which satisfies convergence condition (i) is indicated with a green star on figure 4d. Condition (ii) is satisfied by the selection $(N_\theta, N_\zeta) = (19, 75)$, indicated with a green star, as shown on figure 4e. The fact that this calculation is fast can be seen on figure 4f, taking 33 seconds. Alternative selections of triplets that give fast calculations within the convergence region $\mathcal{R}_5$ are enlisted on table 5.
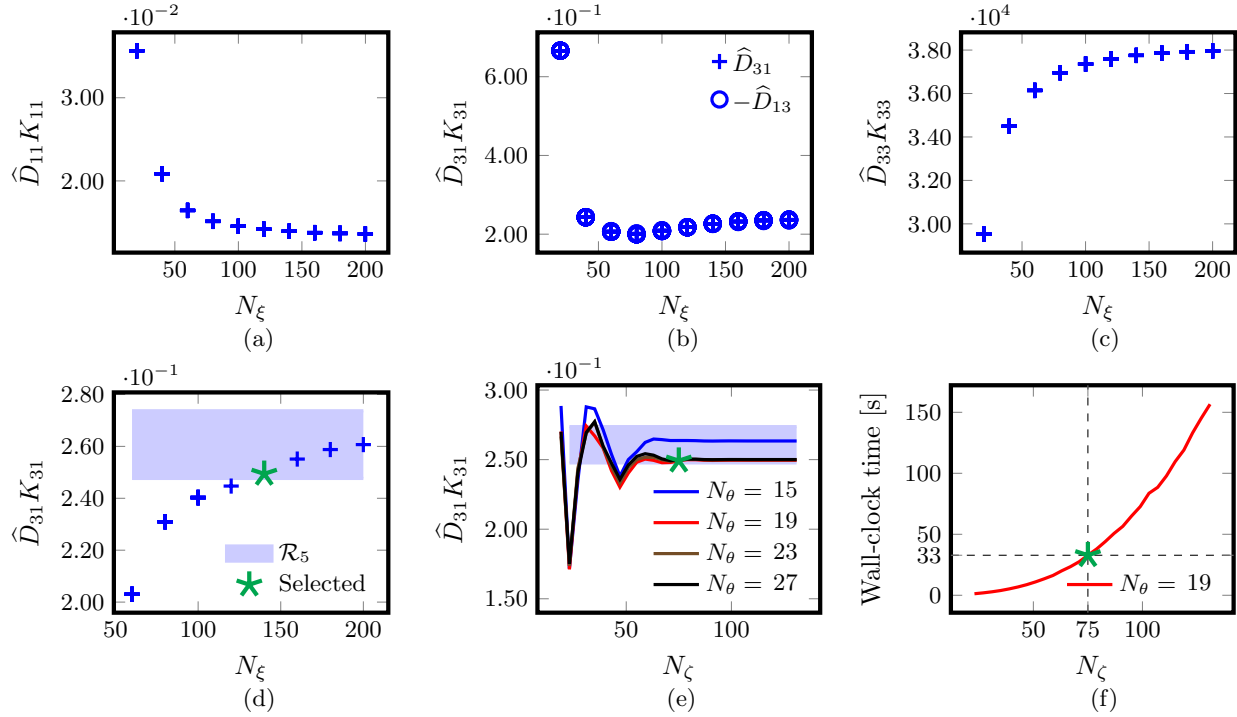
Figure 4: Convergence of monoenergetic coefficients with the number of Legendre modes N_ξ for W7X-KJM at the surface labelled by $\psi/\psi_{\mathrm{lcfs}} = 0.204$, for $\hat{\nu}(v) = 10^{-5}$ m^{-1} and $\hat{E}_r(v) = 3 \cdot 10^{-4}$ kV $\cdot$ s/m^2.

The convergence of monoenergetic coefficients for the nearly quasi-isodynamic configuration CIEMAT-QI in the $1/\nu$ regime is shown in figure 5. It can be seen that convergence in this case requires more Legendre modes than in the rest of cases. From figure 5b we see that the calculation for $N_\xi = 300$ can be used as the converged reference value $\hat{D}_{31}^{\mathrm{r}}$ and we relax the relative convergence parameter to $\epsilon = 8\%$. On figure 5d we see that the region of 8% of deviation $\mathcal{R}_8$ is quite narrow and that selecting $N_\xi = 180$ satisfies condition (i). To satisfy condition (ii) we choose the resolutions $(N_\theta, N_\zeta) = (15, 119)$ as shown in figures 5e and 5f. From figure 5f we can also check that the calculation with the selected resolutions is fast, taking 78 seconds. Additional triplets which lie in the region $\mathcal{R}_8$ and are fast to compute are shown on table 6.

N_θ	N_ζ	N_ξ	t_{clock} [s]
19	75	{180, 200, 220, 240, 260, 280, 300, 320, 340}	{41, 46, 50, 54, 59, 63, 68, 72, 77}
19	99	{160, 180, 200, 220}	{81, 91, 101, 111}
21	99	180	115
15	119	{180, 200, 220, 240}	{78, 86, 95, 104}
19	119	120	100

Table 6: Additional triplets $(N_\theta, N_\zeta, N_\xi)$ that give a fast and accurate calculation of $\hat{D}_{31}$ for CIEMAT-QI at the surface labelled by $\psi/\psi_{\mathrm{lcfs}} = 0.200$, for $\hat{\nu}(v) = 10^{-5}$ m^{-1} and $\hat{E}_r(v) = 0$ kV $\cdot$ s/m^2.
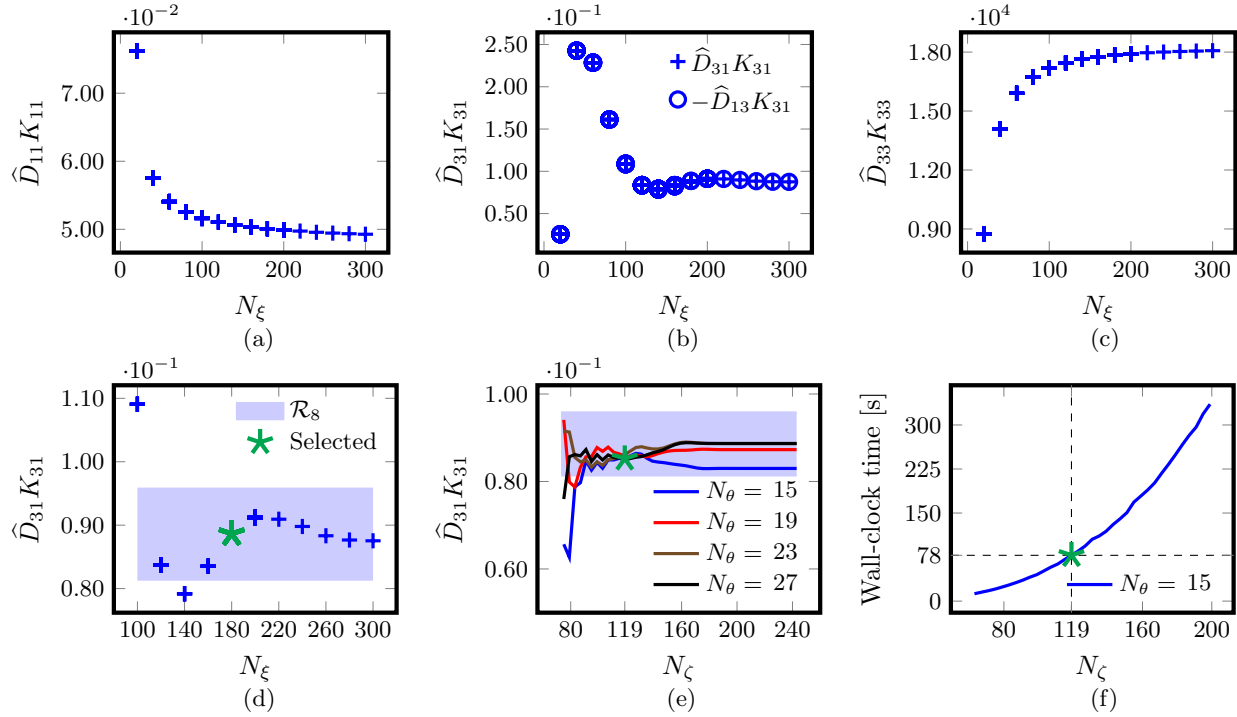
Figure 5: Convergence of monoenergetic coefficients with the number of Legendre modes N_ξ for CIEMAT-QI at the surface labelled by $\psi/\psi_{\text{lcfs}} = 0.25$, for $\hat{\nu}(v) = 10^{-5}$ m^{-1} and $\hat{E}_r(v) = 0$ kV $\cdot$ s/m^2.

For CIEMAT-QI in the $\sqrt{\nu}$ regime, we take the calculation for $N_\xi = 200$ as the converged reference value $\widehat{D}_{31}^{\text{r}}$. We can check from figure 6 that this seems to be a good approximation to the exact converged value of $\widehat{D}_{31}$. From figure 6d we can check that taking $N_\xi = 180$ satisfies condition (i) for the region $\mathcal{R}_8$ of 8% of deviation. As shown in figure 6e, the selection $(N_\theta, N_\zeta) = (15, 119)$ satisfies condition (ii). With this selection, which is the same as for the $1/\nu$ regime, we obtain the same wall-clock time of 78 seconds as can be seen from figure 6f. On table 7, additional selections of the resolutions that also lie in $\mathcal{R}_8$ are enlisted.

4.2. Benchmark of monoenergetic coefficients

As the definition of what means "sufficiently converged" in subsection 4.1 is somewhat arbitrary‖, we need to verify that the resolutions chosen indeed provide sufficiently accurate calculations of all the monoenergetic coefficients. For W7-X, scans in the interval $\hat{\nu} \in [10^{-5}, 300]$ m^{-1} for the $\hat{E}_r$ values in table 1. For CIEMAT-QI, we focus on the low collisionality to plateau interval $\hat{\nu} \in [10^{-5}, 10^{-2}]$. In both cases, MONKES results with the resolutions selected in subsection 4.1 will be benchmarked against fully converged values of the monoenergetic coefficients.

‖ For example, the selection of ϵ could be more stringent or a more accurate value of $\widehat{D}_{31}^{\text{r}}$ could be used.

N_θ	N_ζ	N_ξ	t_{clock} [s]
19	75	{120,140,160}	{27,32,36}
19	99	{160, 180, 200, 220}	{81, 91, 101, 111}
21	75	{120,140,160}	{37,43,49}
21	99	{140,160,180}	{90, 102, 115}
15	119	{120, 140, 160, 180, 200, 220, 240, 260 }	{51, 59, 68, 76, 85, 93, 101, 110 }
19	119	140	116
23	75	{120, 140, 160, 180}	{47, 55, 62, 70}
27	75	{120, 140, 160}	{74, 86, 98}

Table 7: Additional triplets $(N_\theta, N_\zeta, N_\xi)$ that give a fast and accurate calculation of $\widehat{D}_{31}$ for CIEMAT-QI at the surface labelled by $\psi/\psi_{\text{lcfs}} = 0.200$, for $\hat{\nu}(v) = 10^{-5}$ m^{-1} and $\hat{E}_r(v) = 10^{-3}$ kV $\cdot$ s/m^2.

In order to compare the results and the wall-clock time, a similar convergence study has been carried out with DKES. On figures 10, 11 and 12 from Apppendix D, the convergence with the number of Legendre modes of the monoenergetic coefficients calculated by DKES is shown. Additionally, on figures 10b, 10e, 11b, 11e, 12b and 12e we plot the regions of convergence $\mathcal{R}_\epsilon$ for each case. This is done to compare the wall-clock times between MONKES and DKES for the same level of relative convergence with respect to $\widehat{D}_{31}^{\text{r}}$. This comparison is
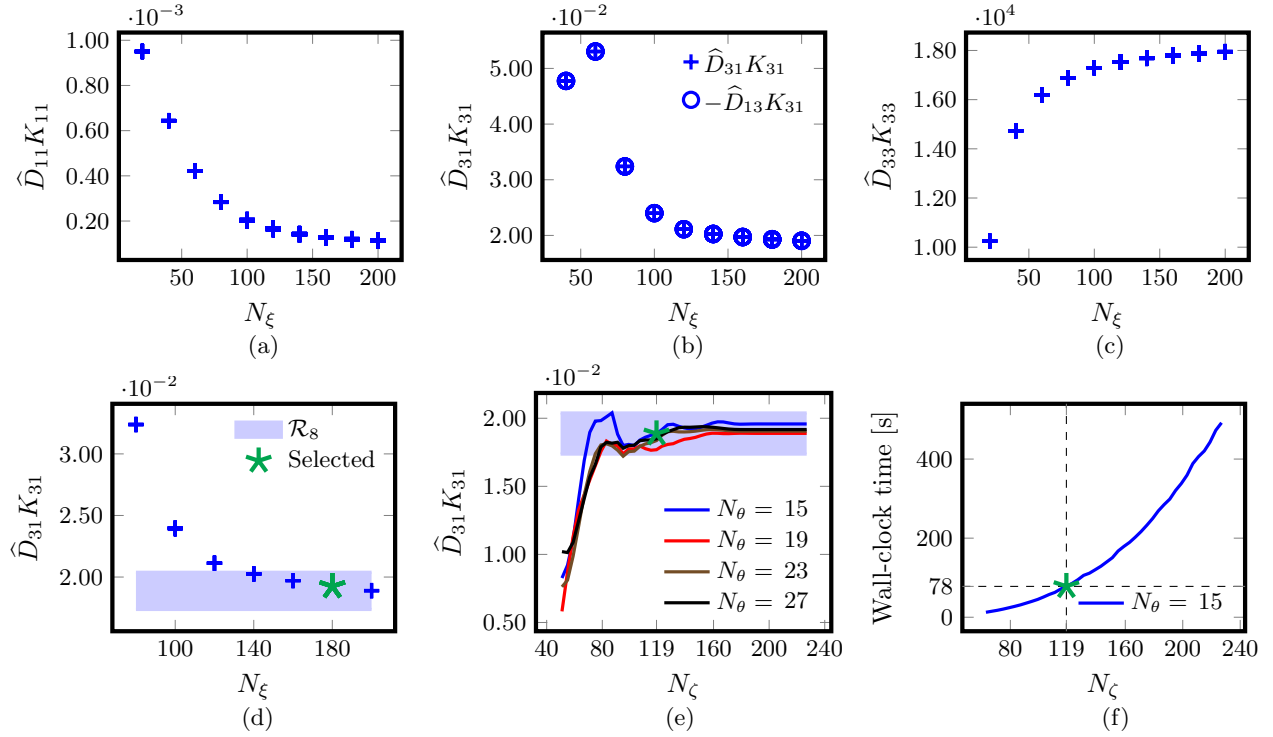
Figure 6: Convergence of monoenergetic coefficients with the number of Legendre modes N_ξ for CIEMAT-QI at the surface labelled by $\psi/\psi_{\text{lcfs}} = 0.25$, for $\hat{\nu}(v) = 10^{-5}$ m^{-1} and $\hat{E}_r(v) = 10^{-3}$ kV $\cdot$ s/m^2.

Case	$N_\xi^{\text{DKES}}\ \epsilon\%$	$t_{\text{clock}}^{\text{DKES}}$ [s]	$t_{\text{clock}}^{\text{MONKES}}$ [s]
W7X-EIM $1/\nu$	80	83.9	22
W7X-EIM $\sqrt{\nu}$	80	57.5	40
W7X-KJM $1/\nu$	120	615	33
W7X-KJM $\sqrt{\nu}$	60	248	33
CIEMAT-QI $1/\nu$	100	238	78
CIEMAT-QI $\sqrt{\nu}$	120	214	78

Table 8: Minimum number of Legendre modes for `DKES` results to satisfy convergence conditions (i) and (ii) and comparison between the wall-clock time of `DKES` and `MONKES`.

displayed on table 8. In all cases, `MONKES` is faster than `DKES`. Even for W7-X EIM, in which we have taken $N_\xi = 80$ for `DKES` calculations, `MONKES` is faster even using twice the number of Legendre modes. For the high mirror configuration, `MONKES` is ~ 20 times faster than `DKES` in the $1/\nu$ regime and ~ 7 times faster than `DKES` in the $\sqrt{\nu}$ regime. In the case of CIEMAT-QI, `MONKES` is not only ~ 3 times faster but we will see it is also more accurate.

For the benchmark, `MONKES` calculations will use the triplets $(N_\theta, N_\zeta, N_\xi)$ selected in subsection 4.1. This calculation of the monoenergetic coefficients will be compared against fully converged calculations from

`DKES` (see Appendix D) and, whenever necessary, from `SFINCS`. The benchmarking of the coefficient $\hat{D}_{11}$ is shown in figure 7. For W7-X, perfect agreement for both the $1/\nu$ and $\sqrt{\nu}$ regimes is obtained. This can be seen from figures 7a and 7b. For CIEMAT-QI however, `DKES` fails to predict the $\sqrt{\nu}$ regime that both `MONKES` and `SFINCS` capture as can be seen on 7c.

Figures 8a and 8b show that `MONKES` calculation of the bootstrap current coefficient for W7-X EIM and W7-X KJM is in total agreement with `DKES` calculation. However, for CIEMAT-QI, `DKES` calculation does not converge to a correct value at low collisionality.
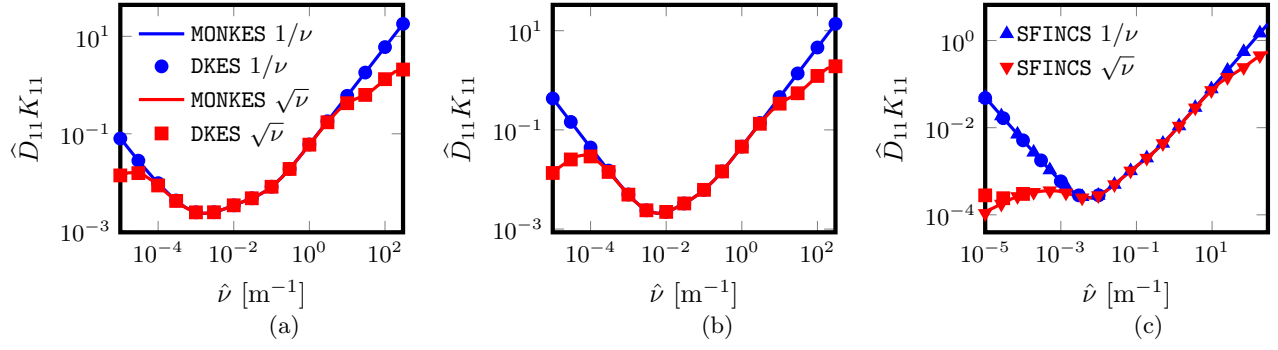
Figure 7: Calculation of $\widehat{D}_{11}$ by `MONKES` and `DKES` in the $1/\nu$ and $\sqrt{\nu}$ regimes. (a) W7-X EIM at the surface $\psi/\psi_{\text{lcfs}} = 0.200$. (b) W7-X KJM at the surface $\psi/\psi_{\text{lcfs}} = 0.204$. (c) CIEMAT-QI at the surface $\psi/\psi_{\text{lcfs}} = 0.250$.
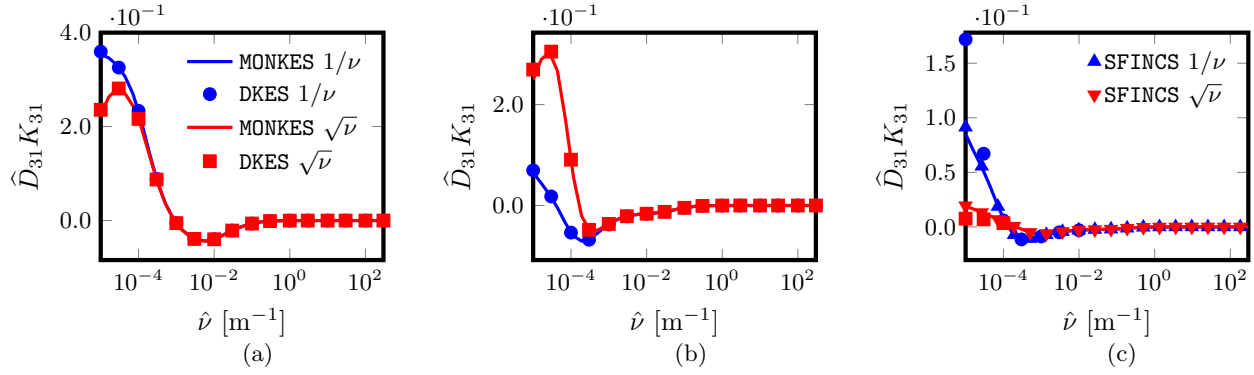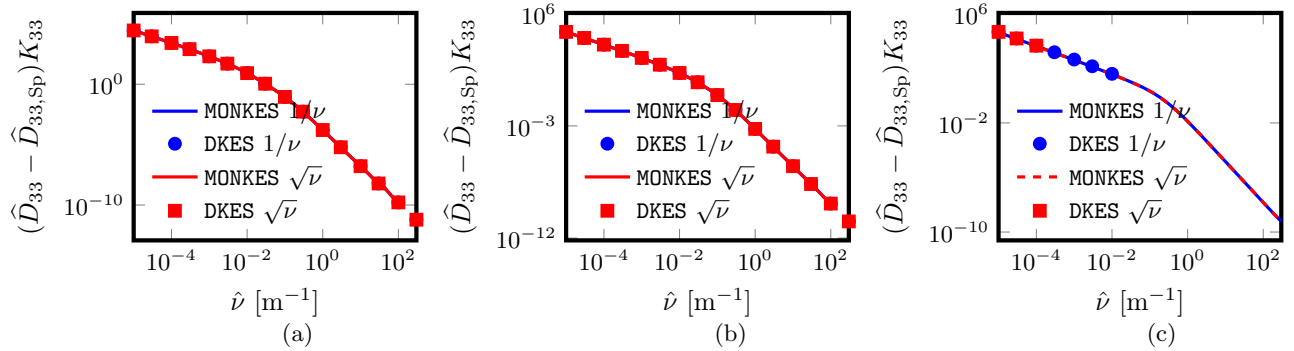

Figure 8: Calculation of $\widehat{D}_{31}$ by `MONKES` and `DKES` in the $1/\nu$ and $\sqrt{\nu}$ regimes. (a) W7-X EIM at the surface $\psi/\psi_{\text{lcfs}} = 0.200$. (b) W7-X KJM at the surface $\psi/\psi_{\text{lcfs}} = 0.204$. (c) CIEMAT-QI at the surface $\psi/\psi_{\text{lcfs}} = 0.250$.

Figure 9: Calculation of $\widehat{D}_{33}$ by `MONKES` and `DKES` in the $1/\nu$ and $\sqrt{\nu}$ regimes. (a) W7-X EIM at the surface $\psi/\psi_{\text{lcfs}} = 0.200$. (b) W7-X KJM at the surface $\psi/\psi_{\text{lcfs}} = 0.204$. (c) CIEMAT-QI at the surface $\psi/\psi_{\text{lcfs}} = 0.250$.

5. Conclusions and future work

– PARALLELIZE MATRIX MULTIPLICATIONS AND INVERSION

– INVERSION WITH GMRES AND PRECONDITIONER BASED ON APPROXIMATING THE SCHUR COMPLEMENTS

– MOMENTUM CONSERVATION

– EXTENSION TO NON STELLARATOR SYMMETRIC IS IMMEDIATE

THIS IS JUST A PARAGRAPH CUT AND PASTED FROM OLD STUFF: An important missing feature of the pitch-angle scattering collision operator used in equation (1) is the lack of parallel momentum conservation, i.e. $\int v\xi\nu^a \mathcal{L}F_a \, \mathrm{d}^3\boldsymbol{v}$ is not identically zero. This lack of conservation introduces an spurious parallel force in the macroscopic momentum equation that can be obtained from kinetic equation (1). Hence, the parallel transport predicted by equation (1) is not correct. Fortunately, there exist techniques (see

e.g. [34] or [35]) to calculate the parallel transport associated to more accurate momentum conserving collision operators by just solving the simplified drift-kinetic equation (17). This has been done successfully in the past by the code PENTA [36, 24] which uses the results of DKES to compute neoclassical transport with a more refined collision operator that preserves momentum.

Appendices

A. Legendre modes of the drift-kinetic equation

Legendre polynomials are the eigenfunctions of the Sturm-Liouville problem in the interval $\xi \in [-1, 1]$ defined by the differential equation

$$2\mathcal{L}P_k(\xi) = -k(k+1)P_k(\xi), \tag{A.1}$$

and regularity boundary conditions at $\xi = \pm 1$

$$(1-\xi^2)\frac{\mathrm{d}P_k}{\mathrm{d}\xi}\bigg|_{\xi=\pm 1} = 0, \tag{A.2}$$

where $k \geq 0$ is an integer.

As $\mathcal{L}$ has a discrete spectrum and is self-adjoint with respect to the inner product

$$\langle f, g \rangle_{\mathcal{L}} := \int_{-1}^{1} fg \, \mathrm{d}\xi, \tag{A.3}$$

in the space of functions that satisfy the regularity condition, $\{P_k\}_{k=0}^{\infty}$ is an orthogonal basis satisfying $\langle P_j, P_k \rangle_{\mathcal{L}} = 2\delta_{jk}/(2k+1)$. Hence, these polynomials satisfy the three-term recurrence formula

$$(2k+1)\xi P_k(\xi) = (k+1)P_{k+1}(\xi) + kP_{k-1}(\xi), \tag{A.4}$$

obtained by Gram-Schmidt orthogonalization, which starting from $P_0 = 1$ and $P_1 = \xi$ defines them all. Additionally, they satisfy the differential identity

$$(1-\xi^2)\frac{\mathrm{d}P_k}{\mathrm{d}\xi} = kP_{k-1}(\xi) - k\xi P_k(\xi). \tag{A.5}$$

Identities (A.4) and (A.5) are useful to represent tridiagonally the left-hand side of equation (17) when we use the expansion (30). The $k-$th Legendre mode of the term $\xi \boldsymbol{b} \cdot \nabla f$ is expressed in terms of the modes $f^{(k-1)}$ and $f^{(k+1)}$ using (A.4)

$$\langle \xi \boldsymbol{b} \cdot \nabla f, P_k \rangle_{\mathcal{L}} = \frac{2}{2k+1}\left[\frac{k}{2k-1}\boldsymbol{b} \cdot \nabla f^{(k-1)}\right.$$
$$\left. + \frac{k+1}{2k+3}\boldsymbol{b} \cdot \nabla f^{(k+1)}\right]. \tag{A.6}$$

Combining both (A.4) and (A.5) allows to express the $k-$th Legendre mode of the mirror term $\nabla \cdot \boldsymbol{b}((1-\xi^2)/2)\,\partial f/\partial \xi$ in terms of the modes $f^{(k-1)}$ and $f^{(k+1)}$ as

$$\left\langle \frac{1}{2}(1-\xi^2)\nabla \cdot \boldsymbol{b}\frac{\partial f}{\partial \xi}, P_k \right\rangle_{\mathcal{L}} = \tag{A.7}$$
$$\frac{\boldsymbol{b} \cdot \nabla \ln B}{2k+1}\left[\frac{k(k-1)}{2k-1}f^{(k-1)} - \frac{(k+1)(k+2)}{2k+3}f^{(k+1)}\right],$$

where we have also used $\nabla \cdot \boldsymbol{b} = -\boldsymbol{b} \cdot \nabla \ln B$. The term proportional to $\hat{E}_{\psi}$ is diagonal in a Legendre representation

$$\left\langle \frac{\hat{E}_{\psi}}{\langle B^2 \rangle}\boldsymbol{B} \times \nabla \psi \cdot \nabla f, P_k \right\rangle_{\mathcal{L}} = \tag{A.8}$$
$$\frac{2}{2k+1}\frac{\hat{E}_{\psi}}{\langle B^2 \rangle}\boldsymbol{B} \times \nabla \psi \cdot \nabla f^{(k)}.$$

Finally, for the collision operator used in equation (17), as Legendre polynomials are eigenfunctions of the pitch-angle scattering operator, using (A.1) we obtain the diagonal representation

$$\langle \hat{\nu}\mathcal{L}f, P_k \rangle_{\mathcal{L}} = -\hat{\nu}\frac{k(k+1)}{2k+1}f^{(k)}. \tag{A.9}$$

B. Invertibility of the spatial differential operators

In this Appendix we will study the invertibility of the left-hand-side of (31). For this, we view L_k, D_k and U_k as operators from $\mathcal{F}$ to $\mathcal{F}$, where $\mathcal{F}$ is the space of smooth functions on the flux-surface equipped with the inner product

$$\langle f, g \rangle_{\mathcal{F}} = \frac{N_p}{4\pi^2}\oint\oint f\bar{g}\,\mathrm{d}\theta\,\mathrm{d}\zeta, \tag{B.1}$$

where $\bar{z}$ denotes the complex conjugate of z and the induced norm

$$\|f\|_{\mathcal{F}} := \sqrt{\langle f, f \rangle_{\mathcal{F}}}. \tag{B.2}$$

In this setting L_k, D_k and U_k are bounded operators from $\mathcal{F}$ to $\mathcal{F}$ as all the coefficients are smooth. The operators L_k and U_k given by (32) and (34) do not have a uniquely defined inverse as they have a non zero kernel. This is a consequence of the fact that the parallel streaming operator

$$\mathcal{V}_{\|} = \xi\boldsymbol{b} \cdot \nabla + \nabla \cdot \boldsymbol{b}\frac{(1-\xi^2)}{2}\frac{\partial}{\partial \xi} \tag{B.3}$$

has a kernel consisting of functions $g((1-\xi^2)/B)$.

To study the invertibility of L_k and U_k we employ coordinates (α, l) where α labels field lines and l is

the magnetic field length. Note that we can study the invertibility of L_k and U_k by studying the existence of solutions to

$$\frac{\mathrm{d}h}{\mathrm{d}l} + a(\alpha, l)h = s(\alpha, l), \qquad (B.4)$$

where $a(\alpha, l)$ and $s(\alpha, l)$ are smooth functions. It is easy to check that the general solution to (B.4) can be written as

$$h(\alpha, l) = (h_0(\alpha) + W(\alpha, l)) \exp(-A(\alpha, l)), \quad (B.5)$$

where

$$A(\alpha, l) = \int_0^l a(\alpha, l')\, \mathrm{d}l', \qquad (B.6)$$

and

$$W(\alpha, l) = \int_0^l s(\alpha, l') \exp(A(\alpha, l'))\, \mathrm{d}l' \qquad (B.7)$$

satisfying $h(\alpha, 0) = h_0(\alpha)$. Thus, the solution to (B.4) in the plane (α, l) is determined up to a constant $h_0(\alpha)$. Imposing continuity on the flux surface to solution (B.5) fixes under some circumstances for $a(\alpha, l)$, the constant h_0. When ι is rational the field line closes on itself after a length L, thus continuity imposes $h(\alpha, l + L) = h(\alpha, l)$. In particular, continuity at $l = 0$ imposes

$$h_0(\alpha) = (h_0(\alpha) + W(\alpha, L)) \exp(-A(\alpha, L)). \quad (B.8)$$

If $A(\alpha, L) \neq 0$, continuity condition (B.8) fixes the value of $h_0(\alpha)$ as

$$h_0(\alpha) = W(\alpha, L) \frac{\exp(-A(\alpha, L))}{1 - \exp(-A(\alpha, L))} \qquad (B.9)$$

An equivalent manner to fix h_0 comes from integrating (B.4) along the field line combined with (B.5). For rational surfaces we integrate in the interval $[0, L]$

$$A(\alpha, L)h_0(\alpha) = \int_0^L s\, \mathrm{d}l - \int_0^L a \exp(-A)W\, \mathrm{d}l \qquad (B.10)$$

which also reveals that when $A(\alpha, L) \neq 0$ equation (B.4) fixes h on the torus completely.

For irrational flux surfaces, we take the limit $L \to \infty$ in condition (B.8) to obtain

$$h_0(\alpha) = h_0(\alpha) \lim_{L \to \infty} \exp(-A(\alpha, L))$$
$$+ \lim_{L \to \infty} W(\alpha, L) \exp(-A(\alpha, L)). \qquad (B.11)$$

Thus, the integration constant h_0 can be determined from (B.11) when $\lim_{L \to \infty} A(\alpha, L) \neq 0$ and the limit $\lim_{L \to \infty} W(\alpha, L) \exp(-A(\alpha, L))$ exists. When it is possible to fix h_0 in irrational surfaces, it is a flux function. A more convenient expression to fix h_0 comes from dividing equation (B.10) by $\int_0^L \mathrm{d}l\, /B$ and taking the limit $L \to \infty$ to obtain

$$\langle Ba \rangle h_0 = \langle Bs \rangle - \langle Ba \exp(-A)W \rangle. \qquad (B.12)$$

Note that if L_k and U_k are written in the form of (B.4), for both the cases, the respective function $a(\alpha, l)$ is proportional to $\partial \ln B / \partial l$. This means that for rational surfaces $A(\alpha, L) = 0$ and when ι is irrational $\lim_{L \to \infty} A(\alpha, L) = 0$ or equivalently $\langle Ba \rangle = 0$. Thus, in both cases, there are infinitely many smooth solutions to (B.4) which proves that L_k and U_k are not one-to-one. Equivalently, all functions of the form $h_0 \exp(-A)$ (for the appropriate A) belong to the kernel of L_k and U_k. Moreover, we obtain conditions on the source $s(\alpha, l)$. For rational surfaces, $W(\alpha, L) = 0$ or equivalently $\int_0^L s\, \mathrm{d}l = \int_0^L a \exp(-A)W\, \mathrm{d}l$ and for irrational surfaces $\lim_{L \to \infty} W(\alpha, L) = 0$ or equivalently $\langle Bs \rangle = \langle Ba \exp(-A)W \rangle$. This means that if we choose a smooth function on the flux surface h and apply either L_k or U_k, the images $L_k h$ or $U_k h$ have to satisfy these extra conditions. This proves that L_k and U_k are not onto. Therefore, they are clearly not invertible.

Now we will prove that if $\hat{\nu} \neq 0$, all the D_k for $k \geq 1$ are invertible. For $\hat{E}_\psi = 0$, D_k is just a multiplication operator and is obviously invertible if $k \neq 0$. When $\hat{E}_\psi \neq 0$ the proof can be done using a similar argument to the one used for L_k and U_k, as we can transform D_k to an equation superficially very similar to (B.4). First, we change from Boozer angles (ψ, θ, ζ) to a different set of magnetic coordinates $(\tilde{\psi}, \alpha, \varphi)$ using the linear transformation

$$\begin{bmatrix} \psi \\ \theta \\ \zeta \end{bmatrix} = \begin{bmatrix} 1 & 0 & 0 \\ 0 & (1 + \iota\delta)^{-1} & \iota \\ 0 & -\delta(1 + \iota\delta)^{-1} & 1 \end{bmatrix} \begin{bmatrix} \tilde{\psi} \\ \alpha \\ \varphi \end{bmatrix} \quad (B.13)$$

where $\delta = B_\theta / B_\zeta$. In these coordinates $\boldsymbol{B} = \nabla\tilde{\psi} \times \nabla\alpha = B_{\tilde{\psi}} \nabla\tilde{\psi} + B_\varphi \nabla\varphi$ and

$$\boldsymbol{B} \times \nabla\tilde{\psi} \cdot \nabla = B^2 \frac{\partial}{\partial \alpha}. \qquad (B.14)$$

Thus, in coordinates (α, φ), the operator D_k takes the form

$$D_k = -\hat{E}_\psi \frac{B^2}{\langle B^2 \rangle} \frac{\partial}{\partial \alpha} + \hat{\nu} \frac{k(k+1)}{2}. \qquad (B.15)$$

Hence, we want to prove that

$$-\hat{E}_\psi \frac{B^2}{\langle B^2 \rangle} \frac{\partial g}{\partial \alpha} + \hat{\nu} \frac{k(k+1)}{2} g = s(\alpha, \varphi) \qquad (B.16)$$

has a unique smooth solution for any source s. The general solution to this equation is

$$g = (g_0(\varphi) + K(\alpha, \varphi)) \exp(A_k(\alpha, \varphi)), \qquad \text{(B.17)}$$

where $g_0(\varphi)$ is an integration constant,

$$K(\alpha, \varphi) = -\frac{\langle B^2 \rangle}{E_\psi}$$
$$\times \int_0^\alpha s(\alpha', \varphi) \exp(-A_k(\alpha', \varphi)) \frac{d\alpha'}{B^2(\alpha', \varphi)} \tag{B.18}$$

and

$$A_k(\alpha, \varphi) = \hat\nu \frac{k(k+1)}{2} \frac{\langle B^2 \rangle}{\hat E_\psi} \int_0^\alpha \frac{d\alpha''}{B^2(\alpha'', \varphi)}. \tag{B.19}$$

Note from (B.13), that the curves of constant φ are straight lines in the (θ, ζ) plane with slope $-\delta$. This means that there are two options if we follow one of these curves: if $\delta \in \mathbb{Q}$ it closes on itself or if $\delta \in \mathbb{R} \backslash \mathbb{Q}$ it densely fills the whole flux surface. Applying the same continuity argument used for (B.5) we obtain that in order to fix g_0 either

$$A_k(L_\alpha, \varphi) \neq 0, \quad \text{if } \delta \in \mathbb{Q}, \tag{B.20}$$
$$\text{or}$$
$$\lim_{\alpha \to \infty} A_k(\alpha, \varphi) \neq 0, \quad \text{if } \delta \in \mathbb{R} \backslash \mathbb{Q}, \tag{B.21}$$

where $L_\alpha > 0$ is the arc-length required for the curve of constant φ to close on itself. However, with the exception of A_0 which is identically zero, A_k is monotonically crescent with α. For $k \geq 1$ we can write the integration constant as

$$g_0(\varphi) = -\frac{K(L_\alpha, \varphi)}{1 - \exp(-A_k(L_\alpha, \varphi))}, \qquad \text{if } \delta \in \mathbb{Q}, \tag{B.22}$$
$$\text{or}$$
$$g_0 = - \lim_{\alpha \to \infty} K(\alpha, \varphi), \qquad \text{if } \delta \in \mathbb{R} \backslash \mathbb{Q}. \tag{B.23}$$

Similarly to the constant h_0, we can obtain equivalent expressions by integrating the differential equation. When $\delta \in \mathbb{Q}$ applying $\int_0^{L_\alpha}$ Eq. (B.16) $d\alpha / B^2$ combined with (B.17) gives

$$g_0(\varphi) = \frac{2}{k(k+1)\hat\nu} \frac{\int_0^{L_\alpha} s \, d\alpha / B^2}{\int_0^{L_\alpha} \exp(A_k) \, d\alpha / B^2}$$
$$- \frac{\int_0^{L_\alpha} K \exp(A_k) \, d\alpha / B^2}{\int_0^{L_\alpha} \exp(A_k) \, d\alpha / B^2} \tag{B.24}$$

Note that the annihilator for $\boldsymbol{B} \times \nabla \tilde\psi \cdot \nabla$ is the flux surface average, i.e. $\left\langle \boldsymbol{B} \times \nabla \tilde\psi \cdot \nabla f \right\rangle = 0$ for any

continuous function on the torus. Using this we can get a more explicit expression for g_0 when $\delta \in \mathbb{R} \backslash \mathbb{Q}$. Taking the flux surface average of (B.16) combined with (B.17) gives

$$g_0 = \frac{2}{k(k+1)\hat\nu} \frac{\langle s \rangle}{\langle \exp(A_k) \rangle} - \frac{\langle K \exp(A_k) \rangle}{\langle \exp(A_k) \rangle}. \tag{B.25}$$

Hence, for $k \geq 1$, we can write the inverse of D_k as the linear operator

$$D_k^{-1} s = (g_0(\varphi) + K(\alpha, \varphi)) \exp(A_k(\alpha, \varphi)),$$

where g_0 is given by (B.24) or (B.25) and is straightforward to check that $D_k D_k^{-1} s = D_k^{-1} D_k s = s$. The operator D_0 is not invertible as it is identically zero for $\hat E_\psi = 0$ and $A_0 = 0$ for $\hat E_\psi \neq 0$.

Finally, we will study the invertibility of the operator Δ_k

$$\Delta_k = D_k - U_k \Delta_{k+1}^{-1} L_{k+1} \tag{B.26}$$

assuming that Δ_{k+1} is bounded and invertible. For this, first, we note that in the space of functions of interest (smooth periodic functions on the torus), using a Fourier basis $\{e^{i(m\theta + nN_p\zeta)}\}_{m,n \in \mathbb{Z}}$, we can approximate any function $f(\theta, \zeta) = \sum_{m,n \in \mathbb{Z}} \hat f_{mn} e^{i(m\theta + nN_p\zeta)} \in \mathcal{F}$ using an approximant $\tilde f(\theta, \zeta)$

$$\tilde f(\theta, \zeta) = \sum_{-N \leq m,n \leq N} \hat f_{mn} e^{i(m\theta + nN_p\zeta)} \tag{B.27}$$

truncating the modes with mode number greater than some positive integer N where

$$\hat f_{mn} = \left\langle f, e^{i(m\theta + nN_p\zeta)} \right\rangle_{\mathcal{F}} \left\| e^{i(m\theta + nN_p\zeta)} \right\|_{\mathcal{F}}^{-2} \tag{B.28}$$

are the Fourier modes of f. Thus, we approximate $\mathcal{F}$ using a finite dimensional subspace $\mathcal{F}^N \subset \mathcal{F}$ consisting on all the functions of the form given by equation (B.27).

Hence, as they are bounded operators, we can approximate D_k, U_k, Δ_{k+1} and L_{k+1} restricted to $\mathcal{F}^N$ (and therefore Δ_k) in equation (B.26) by operators $D_k^N, U_k^N, \Delta_{k+1}^N$ and L_{k+1}^N that map any $\tilde f \in \mathcal{F}^N$ to the projections of $D_k \tilde f, U_k \tilde f, \Delta_{k+1} \tilde f$ and $L_{k+1} \tilde f$ onto $\mathcal{F}^N$. The operators $D_k^N, U_k^N, \Delta_{k+1}^N$ and L_{k+1}^N can be exactly represented (in a Fourier basis) by square matrices of size $\dim \mathcal{F}^N$. When the operators are invertible, these matrices are invertible aswell. Doing so, we can interpret the matrix representation of Δ_k as the Schur complement of the matrix

$$M_k^N = \begin{bmatrix} D_k^N & U_k^N \\ L_{k+1}^N & \Delta_{k+1}^N \end{bmatrix}. \tag{B.29}$$

It is well known from linear algebra that the Schur complement of M_k^N is invertible when both D_k^N and

Δ_{k+1}^N are (which they are). Hence, for $k \geq 1$, the matrix representation of Δ_k^N can be inverted for any N, and therefore Δ_k is invertible. For $k = 0$, it is necessary to substitute one of the rows of $[D_k^N \ U_k^N]$ by the condition (35) so that M_k^N is invertible for any N and as Δ_1^N can be inverted, also Δ_0^N constructed in this manner for any N, which implies that Δ_0 is invertible.

C. Fourier collocation method

In this appendix we describe the Fourier collocation (also called pseudospectral) method for discretizing the angles θ and ζ. This discretization will be used to obtain the matrices $\boldsymbol{L}_k$, $\boldsymbol{D}_k$ and $\boldsymbol{U}_k$. For convenience, we will use the complex version of the discretization method but for the discretization matrices we will just take their real part as the solutions to (17) are all real. We search for approximate solutions to equation (31) of the form

$$f^{(k)}(\theta, \zeta) = \sum_{n=-N_{\zeta 1}/2}^{N_{\zeta 2}/2-1} \sum_{m=-N_{\theta 1}/2}^{N_{\theta 2}/2-1} \tilde{f}_{mn}^{(k)} e^{i(m\theta + nN_p\zeta)}$$

(C.1)

where $N_{\theta 1} = N_\theta - N_\theta \mod 2$, $N_{\theta 2} = N_\theta + N_\theta \mod 2$, $N_{\zeta 1} = N_\zeta - N_\zeta \mod 2$, $N_{\zeta 2} = N_\zeta + N_\zeta \mod 2$ for some positive integers N_θ, N_ζ. The complex numbers

$$\tilde{f}_{mn}^{(k)} := \left\langle f^{(k)}, e^{i(m\theta + nN_p\zeta)} \right\rangle_{N_\theta N_\zeta} \left\| e^{i(m\theta + nN_p\zeta)} \right\|_{N_\theta N_\zeta}^{-2}$$

(C.2)

are the discrete Fourier modes (also called discrete Fourier transform),

$$\langle f, g \rangle_{N_\theta N_\zeta} := \frac{1}{N_\theta N_\zeta} \sum_{j'=0}^{N_\zeta-1} \sum_{i'=0}^{N_\theta-1} f(\theta_{i'}, \zeta_{j'}) \overline{g(\theta_{i'}, \zeta_{j'})},$$

(C.3)

is the discrete inner product associated to the equispaced grid points (46), (47), $\|f\|_{N_\theta N_\zeta} := \sqrt{\langle f, f \rangle_{N_\theta N_\zeta}}$ its induced norm and $\bar{z}$ denotes the complex conjugate of z. We denote by $\mathcal{F}^{N_\theta N_\zeta}$ to the finite dimensional vector space (of dimension $N_\theta N_\zeta$) comprising all the functions that can be written in the form of expansion (C.1).

The set of functions $\{e^{i(m\theta + nN_p\zeta)}\} \subset \mathcal{F}^{N_\theta N_\zeta}$ forms an orthogonal basis for $\mathcal{F}^{N_\theta N_\zeta}$ equipped with the discrete inner product (C.3). Namely,

$$\left\langle e^{i(m\theta + nN_p\zeta)}, e^{i(m'\theta + n'N_p\zeta)} \right\rangle_{N_\theta N_\zeta} \propto \delta_{mm'}\delta_{nn'} \quad \text{(C.4)}$$

for $-N_{\theta 1}/2 \leq m \leq N_{\theta 2}/2$ and $-N_{\zeta 1}/2 \leq n \leq N_{\zeta 2}/2$. Thus, for functions lying in $\mathcal{F}^{N_\theta N_\zeta}$, discrete expansions such as (C.1) coincide with their (finite) Fourier series. The discrete Fourier modes (C.2) are chosen so that the expansion (C.1) interpolates $f^{(k)}$ at grid points. Thus, there is a vector space isomorphism between the space of discrete Fourier modes and $f^{(k)}$ evaluated at the equispaced grid.

Combining equations (C.1), (C.2) and (C.3) we can write our Fourier interpolant as

$$f^{(k)}(\theta, \zeta) = \boldsymbol{I}(\theta, \zeta) \cdot \boldsymbol{f}^{(k)}$$
$$= \sum_{j'=0}^{N_\zeta-1} \sum_{i'=0}^{N_\theta-1} I_{i'j'}(\theta, \zeta) f^{(k)}(\theta_{i'}, \zeta_{j'}), \quad \text{(C.5)}$$

where $\boldsymbol{f}^{(k)} \in \mathbb{R}^{N_{\text{fs}}}$ is the state vector containing $f^{(k)}(\theta_{i'}, \zeta_{j'})$. The entries of the vector $\boldsymbol{I}(\theta, \zeta)$ are the functions $I_{i'j'}(\theta, \zeta)$ given by,

$$I_{i'j'}(\theta, \zeta) = I_{i'}^\theta(\theta) I_{j'}^\zeta(\zeta), \quad \text{(C.6)}$$

$$I_{i'}^\theta(\theta) = \frac{1}{N_\theta} \sum_{m=-N_{\theta 1}/2}^{N_{\theta 2}/2-1} e^{im(\theta-\theta_{i'})}, \quad \text{(C.7)}$$

$$I_{j'}^\zeta(\zeta) = \frac{1}{N_\zeta} \sum_{n=-N_{\zeta 1}/2}^{N_{\zeta 2}/2-1} e^{N_p in(\zeta-\zeta_{j'})}. \quad \text{(C.8)}$$

Note that the interpolant is the only function in $\mathcal{F}^{N_\theta N_\zeta}$ which interpolates the data at the grid points, as $I_{i'}^\theta(\theta_i) = \delta_{ii'}$ and $I_{j'}^\zeta(\zeta_j) = \delta_{jj'}$.

Of course, (C.5) cannot (in general) be a solution to (31) at all points $(\theta, \zeta) \in [0, 2\pi) \times [0, 2\pi/N_p)$. Instead, we will force that (C.5) solves (31) exactly at the equispaced grid points. Thanks to the vector space isomorphism (C.2) between $\boldsymbol{f}^{(k)}$ and the discrete modes $\tilde{f}_{mn}^{(k)}$ this is equivalent to match the discrete Fourier modes of the left and right-hand-sides of equation (31).

Inserting the interpolant (C.5) in the left-hand side of equation (31) and evaluating the result at grid points gives

$$\left(L_k f^{(k-1)} + D_k f^{(k)} + U_k f^{(k)} \right) \Big|_{(\theta_i, \zeta_j)} = \quad \text{(C.9)}$$

$$\left(L_k \boldsymbol{I} \cdot \boldsymbol{f}^{(k-1)} + D_k \boldsymbol{I} \cdot \boldsymbol{f}^{(k)} + U_k \boldsymbol{I} \cdot \boldsymbol{f}^{(k+1)} \right) \Big|_{(\theta_i, \zeta_j)}.$$

Here, $L_k \boldsymbol{I}(\theta_i, \zeta_j)$, $D_k \boldsymbol{I}(\theta_i, \zeta_j)$ and $U_k \boldsymbol{I}(\theta_i, \zeta_j)$ are respectively the rows of $\boldsymbol{L}_k$, $\boldsymbol{D}_k$ and $\boldsymbol{U}_k$ associated to the grid point (θ_i, ζ_j). We can relate them to the actual positions they will occupy in the matrices choosing an ordenation of rows and columns. If we use the ordenation that relates respectively the row i_r and column i_c to the grid points (θ_i, ζ_j) and $(\theta_{i'}, \zeta_{j'})$ as

$$i_r = 1 + i + jN_\theta, \quad \text{(C.10)}$$
$$i_c = 1 + i' + j'N_\theta, \quad \text{(C.11)}$$

for $i, i' = 0, 1, \ldots, N_\theta - 1$ and $j, j' = 0, 1, \ldots, N_\zeta - 1$. With this ordenation, we define the elements of the row i_r and column i_c given by (C.10) and (C.11) of the matrices $\boldsymbol{L}_k$, $\boldsymbol{D}_k$ and $\boldsymbol{U}_k$ to be

$$(\boldsymbol{L}_k)_{i_\mathrm{r} i_\mathrm{c}} = L_k I_{i'j'}(\theta_i, \zeta_j), \qquad (\text{C.12})$$

$$(\boldsymbol{D}_k)_{i_\mathrm{r} i_\mathrm{c}} = D_k I_{i'j'}(\theta_i, \zeta_j), \qquad (\text{C.13})$$

$$(\boldsymbol{U}_k)_{i_\mathrm{r} i_\mathrm{c}} = U_k I_{i'j'}(\theta_i, \zeta_j). \qquad (\text{C.14})$$

Explicitly,

$$
\begin{aligned}
L_k I_{i'j'}\Big|_{(\theta_i,\zeta_j)} &= \frac{k}{2k-1} \left(\boldsymbol{b} \cdot \nabla I_{i'j'}\Big|_{(\theta_i,\zeta_j)} \right. \\
&\left. + \frac{k-1}{2} \, \boldsymbol{b} \cdot \nabla \ln B\Big|_{(\theta_i,\zeta_j)} \delta_{ii'}\delta_{jj'} \right),
\end{aligned}
$$
$$(\text{C.15})$$

$$
\begin{aligned}
D_k I_{i'j'}\Big|_{(\theta_i,\zeta_j)} &= \frac{\hat{E}_\psi}{\langle B^2 \rangle} \, \boldsymbol{B} \times \nabla\psi \cdot \nabla I_{i'j'}\Big|_{(\theta_i,\zeta_j)} \\
&+ \frac{k(k+1)}{2}\hat{\nu}\delta_{ii'}\delta_{jj'},
\end{aligned}
$$
$$(\text{C.16})$$

$$
\begin{aligned}
U_k I_{i'j'}\Big|_{(\theta_i,\zeta_j)} &= \frac{k+1}{2k+3} \left(\boldsymbol{b} \cdot \nabla I_{i'j'}\Big|_{(\theta_i,\zeta_j)} \right. \\
&\left. + \frac{k+2}{2} \, \boldsymbol{b} \cdot \nabla \ln B\Big|_{(\theta_i,\zeta_j)} \delta_{ii'}\delta_{jj'} \right),
\end{aligned}
$$
$$(\text{C.17})$$

where we have used expressions (28) and (29) to write

$$
\begin{aligned}
\boldsymbol{b} \cdot \nabla I_{i'j'}\Big|_{(\theta_i,\zeta_j)} &= \frac{B}{B_\zeta + \iota B_\theta}\Big|_{(\theta_i,\zeta_j)} \\
&\times \left(\iota\delta_{jj'} \frac{\mathrm{d}I_{i'}^\theta}{\mathrm{d}\theta}\Big|_{\theta_i} - \delta_{ii'} \frac{\mathrm{d}I_{j'}^\zeta}{\mathrm{d}\zeta}\Big|_{\zeta_j} \right)
\end{aligned}
$$
$$(\text{C.18})$$

$$
\begin{aligned}
\boldsymbol{B} \times \nabla\psi \cdot \nabla I_{i'j'}\Big|_{(\theta_i,\zeta_j)} &= \frac{B^2}{B_\zeta + \iota B_\theta}\Big|_{(\theta_i,\zeta_j)} \\
&\times \left(B_\zeta\delta_{jj'} \frac{\mathrm{d}I_{i'}^\theta}{\mathrm{d}\theta}\Big|_{\theta_i} - B_\theta\delta_{ii'} \frac{\mathrm{d}I_{j'}^\zeta}{\mathrm{d}\zeta}\Big|_{\zeta_j} \right)
\end{aligned}
$$
$$(\text{C.19})$$

We remark in first place that, for $k = 0$, the rows of $\boldsymbol{D}_0$ and $\boldsymbol{U}_0$ associated to the grid point $(\theta_0, \zeta_0) = (0,0)$, are replaced by equation (35). Finally, each state vector $\boldsymbol{f}^{(k)}$ for the Fourier interpolants contains the images $f^{(k)}(\theta_{i'}, \zeta_{j'})$ at the grid points, ordered according to (C.11).

D. Convergence of monoenergetic coefficients calculated by DKES

In this Appendix we plot how the monoenergetic coefficients calculated by DKES converge. From the output of DKES, the two columns $\widehat{D}_{ij}^\pm$ satisfy $\widehat{D}_{ij}^- \geq \widehat{D}_{ij}^+$ and allow to compute bounds for $\widehat{D}_{ij}$

$$\frac{\widehat{D}_{ij}^- + \widehat{D}_{ij}^+}{2} - \Delta_{ij} \leq \widehat{D}_{ij} \leq \frac{\widehat{D}_{ij}^- + \widehat{D}_{ij}^+}{2} + \Delta_{ij} \quad (\text{D.1})$$

and $\Delta_{ij} = \frac{1}{2}\sqrt{(\widehat{D}_{ii}^- - \widehat{D}_{ii}^+)(\widehat{D}_{jj}^- - \widehat{D}_{jj}^+)}$.
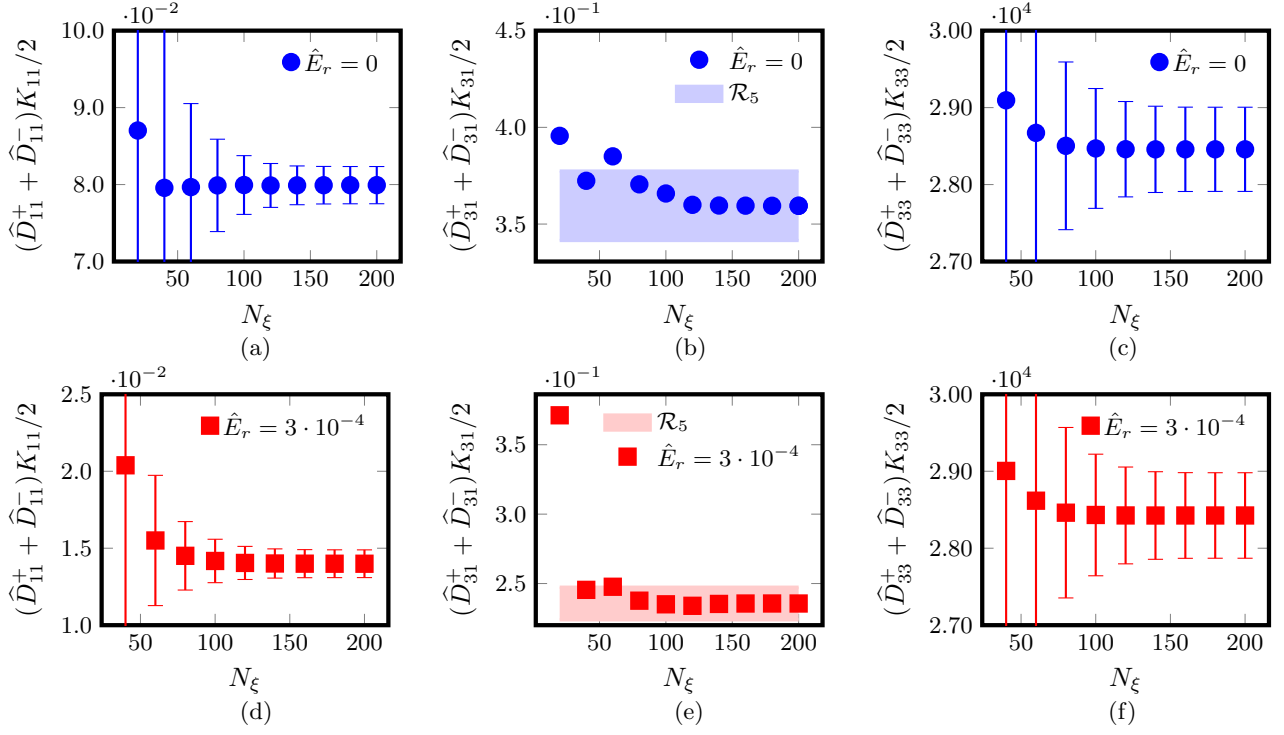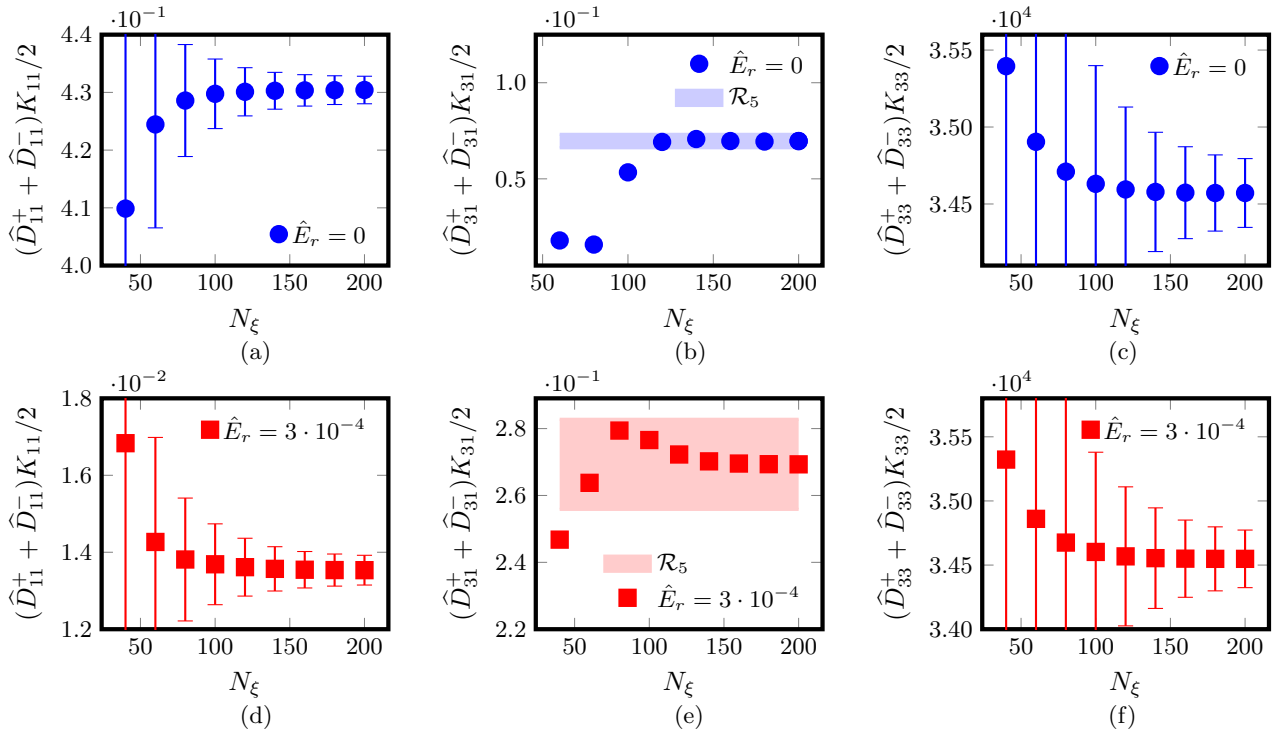
Figure 10: Convergence of monoenergetic coefficients calculated with `DKES` for W7X-EIM at the surface labelled by $\psi/\psi_{\mathrm{lcfs}} = 0.200$. $\hat{E}_r$ in $\mathrm{kV} \cdot \mathrm{s}/\mathrm{m}^2$.

Figure 11: Convergence of monoenergetic coefficients calculated with `DKES` for W7X-KJM at the surface labelled by $\psi/\psi_{\mathrm{lcfs}} = 0.204$. $\hat{E}_r$ in $\mathrm{kV} \cdot \mathrm{s}/\mathrm{m}^2$.
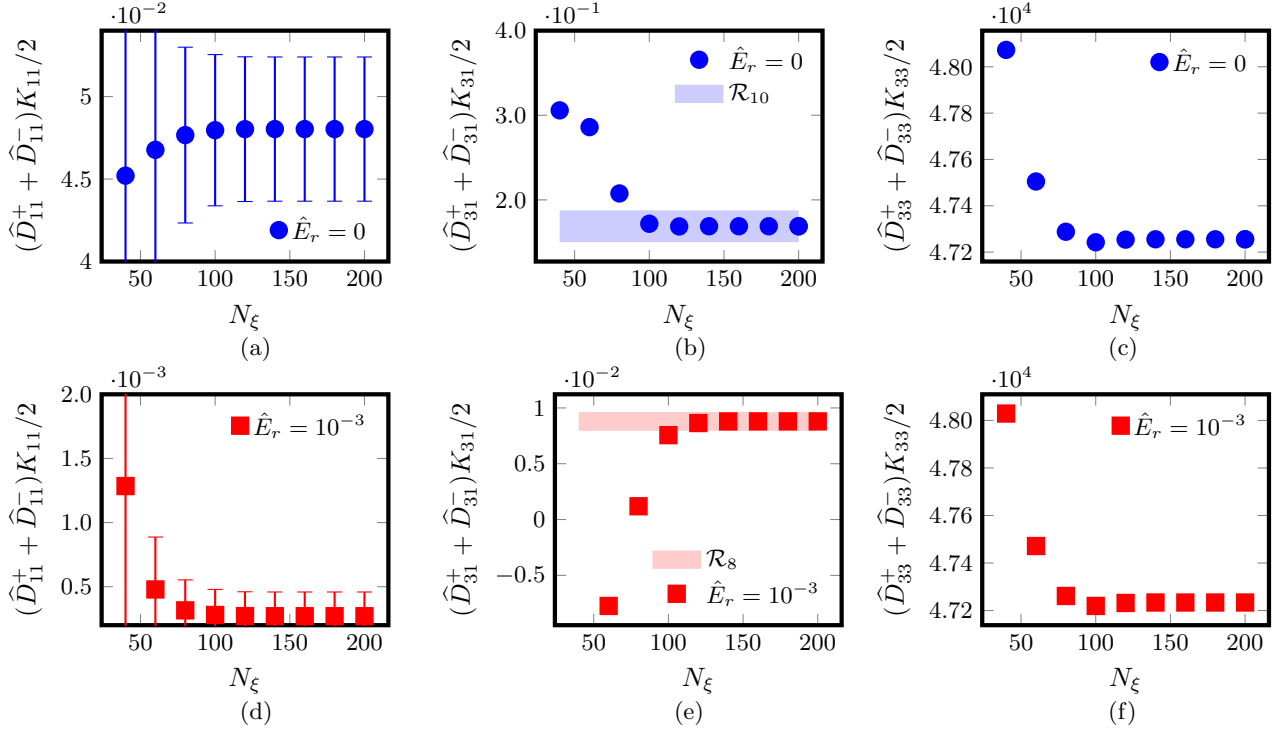
Figure 12: Convergence of monoenergetic coefficients calculated with DKES for CIEMAT-QI at the surface labelled by $\psi/\psi_{\mathrm{lcfs}} = 0.250$. $\hat{E}_r$ in $\mathrm{kV} \cdot \mathrm{s/m^2}$.

Acknowledgements

References

[1] Per Helander. Theory of plasma confinement in non-axisymmetric magnetic fields. *Reports on Progress in Physics*, 77(8):087001, jul 2014.

[2] A. Pytte and Allen H. Boozer. Neoclassical transport in helically symmetric plasmas. *The Physics of Fluids*, 24(1):88–92, 01 1981.

[3] Allen H. Boozer. Transport and isomorphic equilibria. *The Physics of Fluids*, 26(2):496–499, 02 1983.

[4] Matt Landreman and Elizabeth Paul. Magnetic fields with precise quasisymmetry for plasma confinement. *Phys. Rev. Lett.*, 128:035001, Jan 2022.

[5] C. D. Beidler, H. M. Smith, A. Alonso, T. Andreeva, J. Baldzuhn, M. N. A. Beurskens, M. Borchardt, S. A. Bozhenkov, K. J. Brunner, H. Damm, M. Drevlak, O. P. Ford, G. Fuchert, J. Geiger, P. Helander, U. Hergenhahn, M. Hirsch, U. Höfel, Ye. O. Kazakov, R. Kleiber, M. Krychowiak, S. Kwak, A. Langenberg, H. P. Laqua, U. Neuner, N. A. Pablant, E. Pasch, A. Pavone, T. S. Pedersen, K. Rahbarnia, J. Schilling, E. R. Scott, T. Stange, J. Svensson, H. Thomsen, Y. Turkin, F. Warmer, R. C. Wolf, D. Zhang, I. Abramovic, S. Äkäslompolo, J. Alcusón, P. Aleynikov, K. Aleynikova, A. Ali, G. Anda, E. Ascasibar, J. P. Bähner, S. G. Baek, M. Balden, M. Banduch, T. Barbui, W. Behr, A. Benndorf, C. Biedermann, W. Biel, B. Blackwell, E. Blanco, M. Blatzheim, S. Ballinger, T. Bluhm, D. Böckenhoff, B. Böswirth, L.-G. Böttger, V. Borsuk, J. Boscary, H.-S. Bosch, R. Brakel, H. Brand, C. Brandt, T. Bräuer, H. Braune, S. Brezinsek, K.-J. Brunner, R. Burhenn, R. Bussiahn, B. Buttenschön, V. Bykov, J. Cai, I. Calvo, B. Cannas, A. Cappa, A. Carls, L. Carraro, B. Carvalho, F. Castejon, A. Charl, N. Chaudhary, D. Chauvin, F. Chernyshev, M. Cianciosa, R. Citarella, G. Claps, J. Coenen, M. Cole, M. J. Cole, F. Cordella, G. Cseh, A. Czarnecka, K. Czerski, M. Czerwinski, G. Czymek, A. da Molin, A. da Silva, A. de la Pena, S. Degenkolbe, C. P. Dhard, M. Dibon, A. Dinklage, T. Dittmar, P. Drewelow, P. Drews, F. Durodie, E. Edlund, F. Effenberg, G. Ehrke, S. Elgeti, M. Endler, D. Ennis, H. Esteban, T. Estrada, J. Fellinger, Y. Feng, E. Flom, H. Fernandes, W. H. Fietz, W. Figacz, J. Fontdecaba, T. Fornal, H. Frerichs, A. Freund, T. Funaba, A. Galkowski, G. Gantenbein, Y. Gao, J. García Regaña, D. Gates, B. Geiger, V. Giannella, A. Gogoleva, B. Goncalves, A. Goriaev, D. Gradic, M. Grahl, J. Green, H. Greuner, A. Grosman, H. Grote, M. Gruca, O. Grulke, C. Guerard, P. Hacker, X. Han, J. H. Harris, D. Hartmann, D. Hathiramani, B. Hein, B. Heinemann, S. Henneberg, M. Henkel, J. Hernandez Sanchez, C. Hidalgo, K. P. Hollfeld, A. Hölting, D. Höschen, M. Houry, J. Howard, X. Huang, Z. Huang, M. Hubeny, M. Huber, H. Hunger, K. Ida, T. Ilkei, S. Illy, B. Israeli, S. Jablonski, M. Jakubowski, J. Jelonnek, H. Jenzsch, T. Jesche, M. Jia, P. Junghanns, J. Kacmarczyk, J.-P. Kallmeyer, U. Kamionka, H. Kasahara, W. Kasparek, N. Kenmochi, C. Killer, A. Kirschner, T. Klinger, J. Knauer, M. Knaup, A. Knieps, T. Kobarg, G. Kocsis, F. Köchl, Y. Kolesnichenko, A. Könies, R. König, P. Kornejew, J.-P. Koschinsky, F. Köster, M. Krämer, R. Krampitz, A. Krämer-Flecken, N. Krawczyk, T. Kremeyer, J. Krom, I. Ksiazek, M. Kubkowska, G. Kühner, T. Kurki-Suonio, P. A. Kurz, M. Landreman, P. Lang, R. Lang, S. Langish, H. Laqua, R. Laube, S. Lazerson, C. Lechte, M. Lennartz, W. Leonhardt, C. Li, Y. Li, Y. Liang, C. Linsmeier, S. Liu, J.-F. Lobsien, D. Loesser, J. Loizu Cisquella, J. Lore,

A. Lorenz, M. Losert, A. Lücke, A. Lumsdaine, V. Lutsenko, H. Maßberg, O. Marchuk, J. H. Matthew, S. Marsen, M. Marushchenko, S. Masuzaki, D. Maurer, M. Mayer, K. McCarthy, P. McNeely, A. Meier, D. Mellein, B. Mendelevitch, P. Mertens, D. Mikkelsen, A. Mishchenko, B. Missal, J. Mittelstaedt, T. Mizuuchi, A. Mollen, V. Moncada, T. Mönnich, T. Morisaki, D. Moseev, S. Murakami, G. Náfrádi, M. Nagel, D. Naujoks, H. Neilson, R. Neu, O. Neubauer, T. Ngo, D. Nicolai, S. K. Nielsen, H. Niemann, T. Nishizawa, R. Nocentini, C. Nührenberg, J. Nührenberg, S. Obermayer, G. Offermanns, K. Ogawa, J. Ölmanns, J. Ongena, J. W. Oosterbeek, G. Orozco, M. Otte, L. Pacios Rodriguez, N. Panadero, N. Panadero Alvarez, D. Papenfuß, S. Paqay, E. Pawelec, G. Pelka, V. Perseo, and the W7-X Team. Demonstration of reduced neoclassical energy transport in wendelstein 7-x. *Nature*, 596(7871):221–226, Aug 2021.

[6] P Helander and J Nührenberg. Bootstrap current and neoclassical transport in quasi-isodynamic stellarators. *Plasma Physics and Controlled Fusion*, 51(5):055004, feb 2009.

[7] P. Helander, J. Geiger, and H. Maßberg. On the bootstrap current in stellarators and tokamaks. *Physics of Plasmas*, 18(9), 09 2011. 092505.

[8] H Peraza-Rodriguez, J M Reynolds-Barredo, R Sanchez, V Tribaldos, and J Geiger. Bootstrap current control studies in the wendelstein 7-x stellarator using the free-plasma-boundary version of the siesta mhd equilibrium code. *Plasma Physics and Controlled Fusion*, 60(2):025023, jan 2018.

[9] E. Sánchez, J.L. Velasco, I. Calvo, and S. Mulas. A quasi-isodynamic configuration with good confinement of fast ions at low plasma beta. *Nuclear Fusion*, 63(6):066037, may 2023.

[10] R. Jorge, G.G. Plunk, M. Drevlak, M. Landreman, J.-F. Lobsien, K. Camacho Mata, and P. Helander. A single-field-period quasi-isodynamic stellarator. *Journal of Plasma Physics*, 88(5):175880504, 2022.

[11] Katia Camacho Mata, Gabriel G. Plunk, and Rogerio Jorge. Direct construction of stellarator-symmetric quasi-isodynamic magnetic configurations. *Journal of Plasma Physics*, 88(5):905880503, 2022.

[12] Alan Goodman, Katia Camacho Mata, Sophia A Henneberg, Rogerio Jorge, Matt Landreman, Gabriel Plunk, Hakan Smith, Ralf Mackenbach, and Per Helander. Constructing precisely quasi-isodynamic magnetic fields, 2022.

[13] Daniel W. Dudt, Alan G. Goodman, Rory Conlin, Dario Panici, and Egemen Kolemen. Magnetic fields with general omnigenity, 2023.

[14] Iván Calvo, Felix I Parra, José Luis Velasco, and J Arturo Alonso. The effect of tangential drifts on neoclassical transport in stellarators close to omnigeneity. *Plasma Physics and Controlled Fusion*, 59(5):055014, mar 2017.

[15] Vincent d'Herbemont, Felix I. Parra, Iván Calvo, and José Luis Velasco. Finite orbit width effects in large aspect ratio stellarators. *Journal of Plasma Physics*, 88(5):905880507, 2022.

[16] J.L. Velasco, I. Calvo, F.I. Parra, and J.M. García-Regaña. Knosos: A fast orbit-averaging neoclassical code for stellarator geometry. *Journal of Computational Physics*, 418:109512, 2020.

[17] J.L. Velasco, I. Calvo, F.I. Parra, V. d'Herbemont, H.M. Smith, D. Carralero, T. Estrada, and the W7-X Team. Fast simulations for large aspect ratio stellarators with the neoclassical code knosos. *Nuclear Fusion*, 61(11):116013, sep 2021.

[18] Viktor V. Nemov, Sergei V. Kasilov, Winfried Kernbichler, and Martin F. Heyn. Evaluation of $1/\nu$ neoclassical transport in stellarators. *Physics of Plasmas*, 6:4622–4632, 1999.

[19] Samuel Lazerson, John Schmitt, Caoxiang Zhu, Joshua Breslau, All STELLOPT Developers, and USDOE Office of Science. Stellopt, version 2.7.5, 5 2020.

[20] K. C. Shaing and J. D. Callen. Neoclassical flows and transport in nonaxisymmetric toroidal plasmas. *The Physics of Fluids*, 26(11):3315–3326, 11 1983.

[21] N. Nakajima, M. Okamoto, J. Todoroki, Y. Nakamura, and M. Wakatani. Optimization of bootstrap current in a large helical system with L = 2, August 1988.

[22] P. Helander, F. I. Parra, and S. L. Newton. Stellarator bootstrap current and plasma flow velocity at low collisionality. *Journal of Plasma Physics*, 83(2):905830206, 2017.

[23] M. Landreman, S. Buller, and M. Drevlak. Optimization of quasi-symmetric stellarators with self-consistent bootstrap current and energetic particle confinement. *Physics of Plasmas*, 29(8), 08 2022. 082501.

[24] H. Sugama and S. Nishimura. How to calculate the neoclassical viscosity, diffusion, and current coefficients in general toroidal plasmas. *Physics of Plasmas*, 9(11):4637–4653, 10 2002.

[25] W. I. van Rij and S. P. Hirshman. Variational bounds for transport coefficients in three-dimensional toroidal plasmas. *Physics of Fluids B: Plasma Physics*, 1(3):563–569, 1989.

[26] M. Landreman, H. M. Smith, A. Mollén, and P. Helander. Comparison of particle trajectories and collision operators for collisional transport in nonaxisymmetric plasmas. *Physics of Plasmas*, 21(4):042503, 2014.

[27] P Helander and DJ Sigmar. *Collisional transport in magnetized plasmas*. Cambridge university press, 2005.

[28] S. P. Hirshman, K. C. Shaing, W. I. van Rij, C. O. Beasley, and E. C. Crume. Plasma transport coefficients for nonsymmetric toroidal confinement systems. *The Physics of Fluids*, 29(9):2951–2959, 1986.

[29] C.D. Beidler, K. Allmaier, M.Yu. Isaev, S.V. Kasilov, W. Kernbichler, G.O. Leitold, H. Maßberg, D.R. Mikkelsen, S. Murakami, M. Schmidt, D.A. Spong, V. Tribaldos, and A. Wakasa. Benchmarking of the mono-energetic transport coefficients—results from the international collaboration on neoclassical transport in stellarators (icnts). *Nuclear Fusion*, 51(7):076001, jun 2011.

[30] Matt Landreman. The monoenergetic approximation in stellarator neoclassical calculations. *Plasma Physics and Controlled Fusion*, 53(8):082003, jun 2011.

[31] Lloyd N. Trefethen and J. A. C. Weideman. The exponentially convergent trapezoidal rule. *SIAM Review*, 56(3):385–458, 2014.

[32] E. Anderson, Z. Bai, C. Bischof, S. Blackford, J. Demmel, J. Dongarra, J. Du Croz, A. Greenbaum, S. Hammarling, A. McKenney, and D. Sorensen. *LAPACK Users' Guide*. Society for Industrial and Applied Mathematics, Philadelphia, PA, third edition, 1999.

[33] J. L. Tennyson, John R. Cary, and D. F. Escande. Change of the adiabatic invariant due to separatrix crossing. *Phys. Rev. Lett.*, 56:2117–2120, May 1986.

[34] M. Taguchi. A method for calculating neoclassical transport coefficients with momentum conserving collision operator. *Physics of Fluids B: Plasma Physics*, 4(11):3638–3643, 11 1992.

[35] H. Maßberg, C. D. Beidler, and Y. Turkin. Momentum correction techniques for neoclassical transport in stellarators. *Physics of Plasmas*, 16(7), 07 2009. 072504.

[36] D. A. Spong. Generation and damping of neoclassical plasma flows in stellaratorsa). *Physics of Plasmas*, 12(5), 04 2005. 056114.